

# A survey of 25 years' transpolar voltage data from the SuperDARN radar network and the Expanding-Contracting Polar Cap model

Michael Lockwood<sup>1,1</sup> and Kathryn A McWilliams<sup>2,2</sup>

<sup>1</sup>University of Reading

<sup>2</sup>University of Saskatchewan

November 30, 2022

## Abstract

We use 214410 hourly observations of the transpolar voltage,  $\Phi_{PC}$ , from 25 years of observations by the SuperDARN radars, to confirm the central tenet of the Expanding-Contracting Polar Cap (ECPC) model of ionospheric convection that  $\Phi_{PC}$  responds to both dayside and nightside reconnection voltages ( $\Phi_D$  and  $\Phi_N$ ). We show  $\Phi_{PC}$  increases at a fixed level of nightside auroral electrojet AL index with increasingly southward IMF (identifying the well-known effect of  $\Phi_D$  on  $\Phi_{PC}$ ) but also with increasingly negative AL at a fixed southward IMF (identifying a distinct effect of  $\Phi_N$  on  $\Phi_{PC}$ ). We study the variation of  $\Phi_{PC}$  with time elapsed  $\Delta t$  since the IMF last pointed southward and show that low/large values occur when -AL is small/large. We have to allow for the fact that at lower numbers of radar echoes,  $n_e$ , the matched potential re-analysis technique used to derive is influenced by the model used: this is done by a sensitivity study of the threshold of  $n_e$  required. We show that for any threshold  $\Phi_{PC}$  falls to about 15kV for  $\Delta t$  greater than about 15 hours giving an upper limit to the viscous-like voltage. It is shown that both  $\Phi_{PC}$  and

-AL  $\epsilon\kappa\epsilon\alpha\sigma\epsilon$   $\omega\iota\tau\eta$   $\epsilon\kappa\epsilon\alpha\sigma\epsilon\delta$   $\sigma\omicron\lambda\alpha\rho$   $\omega\iota\kappa\delta$   $\delta\psi\eta\alpha\mu\iota\varsigma$   $\pi\epsilon\sigma\sigma\upsilon\rho\epsilon$   $\pi\sigma\omega$ ,  $\beta\upsilon\tau$   $\nu\omicron\tau$   $\alpha\varsigma$   $\mu\upsilon\varsigma\eta$   $\alpha\varsigma$   $\tau\eta\epsilon$   $\mu\iota\delta$ - $\lambda\alpha\tau\iota\tau\upsilon\delta\epsilon$   $\gamma\epsilon\omicron\mu\alpha\gamma\eta\epsilon\tau\iota\varsigma$   $\rho\alpha\eta\gamma\epsilon$   $\epsilon\kappa\delta\epsilon\zeta$   $\alpha\mu$ .  $\Omega\epsilon$   $\varsigma\omicron\kappa\lambda\upsilon\delta\epsilon$   $\pi\sigma\omega$ ,  $\epsilon\kappa\epsilon\alpha\sigma\epsilon\varsigma$   $\beta\omicron\tau\eta$   $\Phi$ .

## **A survey of 25 years' transpolar voltage data from the SuperDARN radar network and the Expanding-Contracting Polar Cap model**

Mike Lockwood<sup>1</sup> and Kathryn A. McWilliams<sup>2</sup>

<sup>1</sup> *Department of Meteorology, University of Reading, Earley Gate, Reading, RG6 6BB, UK*

<sup>2</sup> *Institute of Space and Atmospheric Studies, University of Saskatchewan, Saskatoon, Saskatchewan, S7N 5E2, Canada*

**Abstract.** We use 214410 hourly observations of transpolar voltage,  $\Phi_{PC}$ , from 25 years' observations by the SuperDARN radars to confirm the central tenet of the Expanding-Contracting Polar Cap model of ionospheric convection that  $\Phi_{PC}$  responds to both dayside and nightside reconnection voltages ( $\Phi_D$  and  $\Phi_N$ ). We show  $\Phi_{PC}$  increases at a fixed level of the nightside auroral electrojet  $AL$  index with increasingly southward IMF (identifying the well-known effect of  $\Phi_D$  on  $\Phi_{PC}$ ) but also with increasingly negative  $AL$  at a fixed southward IMF (identifying a distinct effect of  $\Phi_N$  on  $\Phi_{PC}$ ). We also study the variation of  $\Phi_{PC}$  with time elapsed  $\Delta t$  since the IMF last pointed southward and show low/large values occur when  $(-AL)$  is small/large. Lower numbers of radar echoes,  $n_e$ , mean that the “map-potential” re-analysis technique used to derive  $\Phi_{PC}$  is influenced by the model used: we present a sensitivity study of the effect of the threshold of  $n_e$  required to avoid this. We show that for any threshold  $n_e$ ,  $\Phi_{PC}$  falls to about 15 kV for  $\Delta t$  greater than about 15 hours, indicating any viscous-like voltage  $\Phi_V$  is considerably smaller than this. It is shown that both  $\Phi_{PC}$  and  $(-AL)$  increase with increased solar wind dynamic pressure  $p_{SW}$ , but not as much as the mid-latitude geomagnetic index  $am$ . We conclude  $p_{SW}$  increases both  $\Phi_D$  and  $\Phi_N$  through increasing the magnetic shear across the relevant current sheet but has a larger effect on mid-latitude geomagnetic indices because of the effect of additional energy stored in the tail lobes.

## 1. Introduction.

This paper studies the Expanding-Contracting Polar Cap (ECPC) model of ionospheric convection excitation (*Cowley and Lockwood, 1992*) using an unprecedentedly large dataset of observations of the transpolar voltage  $\Phi_{PC}$ , also known as the cross-cap potential difference. The ECPC model predicts that  $\Phi_{PC}$  at any one instant depends on the reconnection voltage in the cross-tail current sheet  $\Phi_N$  as well as that at the dayside magnetopause  $\Phi_D$ .

One specific aim is to re-create two scatter plots from surveys of  $\Phi_{PC}$  that have been of great importance to our understanding of the excitation of ionospheric polar convection by the solar wind flow, but here using a very much larger dataset of observations. The first of these scatter plots shows the dependence of  $\Phi_{PC}$  on the northward component  $B_Z$  of the Interplanetary Magnetic Field (IMF) in the Geocentric Solar Magnetospheric (GSM) reference frame (*Reiff et al., 1981; Cowley, 1984; Boyle, 1997; Hairston et al., 1998; Milan et al., 2004; Liu et al., 2019*). The second scatter plot shows the dependence of  $\Phi_{PC}$  during northward IMF ( $B_Z > 0$ ) on the time elapsed since the IMF was last southward (*Wygant et al., 1983*). We also aim to use the large dataset, which covers more than a whole Hale solar magnetic cycle, to extend our understanding of the separate effects of reconnection in the magnetopause and the cross-tail current sheet by comparisons with the behaviour of the  $AL$  auroral electrojet index and to investigate the separate effects of solar wind dynamic pressure on  $\Phi_D$  and  $\Phi_N$ .

### 1-i. Transpolar voltage, steady state and non-steady-state convection

Magnetospheric convection (the circulation of plasma and frozen-in magnetic field) is at the heart of our understanding of the response of geomagnetic activity and terrestrial space weather to the transfer of energy from the solar wind into the magnetosphere. Directly-driven geomagnetic responses, historically called “Disturbance Polar-2” or “DP-2”, are usually dominated by eastward currents in the afternoon sector polar ionosphere and detected as positive enhancements of the  $AU$  auroral electrojet index. DP-2 currents correlate highly with solar wind forcing at short response delays (*Nishida, 1968a; b; Lockwood et al., 1986; Etemadi et al., 1988; Todd et al., 1988*). These are driven responses to magnetic reconnection in the dayside magnetopause current sheet which generates open magnetospheric field lines (*Consolini and De Michelis, 2005; Finch et al., 2008; Echer et al., 2017*), the voltage  $\Phi_D$  being the magnetic flux transfer rate from the closed to open magnetospheric field-line

topology. The open field lines generated are swept into the geomagnetic tail by the solar wind flow where they accumulate, storing energy there. These open field lines in the tail are subsequently re-closed in bursts of reconnection in the cross-tail current sheet, giving the storage-release responses of geomagnetic activity (“DP-1”) after a longer lag time than for the DP-2 response (*Baker et al.*, 1983; *McPherron et al.*, 1998; *Klimas et al.*, 1992; 1994; *Finch et al.*, 2008). The DP-1 response is dominated by the effects of the westward auroral electrojet current across midnight in the substorm current wedge and seen as negative perturbations of the *AL* auroral electrojet index. The voltage  $\Phi_N$  is the magnetic flux transfer rate from the open to the closed magnetospheric field-line topology. The storage-release response is often described in terms of the magnetospheric substorm cycle (e.g., *Baker et al.*, 1997; *McPherron et al.*, 1998). A review of the development of our understanding of the relationship of magnetospheric flux transport, the Dungey convection cycle and substorms has been given by *McPherron* (2020) and a review of the associated energy flow through the magnetosphere has been given by *Lockwood* (2019).

Being at the foot of magnetospheric field lines and, like the magnetosphere, being of high magnetic Reynolds number, the frozen-in flux theorem applies in the polar ionospheric F-region and topside ionosphere. Hence these regions reflect the circulation of frozen-in flux in the magnetosphere (ionospheric convection). However, there is one key difference between the flows in the magnetosphere and in the ionosphere. The magnetosphere is compressible, a fact that the storage-release system depends upon. On the other hand, the ionosphere is incompressible, in the sense that the magnetic field there is constant to within a very small factor, such that even a very large geomagnetic disturbance is only a very small fraction of the intrinsic geomagnetic field (for example, 1000 nT is less than a 2% perturbation). The reason for this is the ionosphere’s close proximity to the currents in the Earth’s interior that generate the geomagnetic field. This difference means that during substorm growth phases, when energy is accumulating in the near-Earth lobes of the magnetospheric geomagnetic tail because the field there is growing (and to some extent also because the lobes are expanding in cross-sectional area as the tail flares), the ionospheric footprint of the open field lines of the lobes (the open polar caps) must be expanding in area (*Holzer et al.*, 1986; *Lockwood et al.*, 1990; *Lockwood and Cowley*, 1992; *Milan et al.*, 2003; 2009; 2012; *Huang et al.*, 2009). *Siscoe and Huang* (1985) showed how expanding “adiarctic” segments polar cap boundaries (meaning “not flowing across”, i.e., not mapping to a magnetospheric reconnection site)

would influence the pattern of ionospheric convection. This concept was used by *Cowley and Lockwood* (1992) to show how ionospheric convection is driven by both the generation and destruction of open flux (the “Expanding-Contracting Polar Cap”, ECPC model). This is different to the magnetosphere, where flows are driven by the solar wind flow, pressure balance and the magnetohydrodynamic (MHD) curvature force that acts to straighten bent field lines. The ECPC concept is supported by detailed comparisons between theory and observations of how patches of newly-opened flux, generated by magnetopause reconnection bursts, evolve poleward (*Cowley et al.*, 1991a; *Lockwood et al.*, 1993; *McWilliams et al.*, 2000; *Throp et al.*, 2005; *Lockwood et al.*, 2006). The result of these considerations is that ionospheric convection is not, in general, a straightforward image of the magnetospheric circulation and the two are decoupled by induction effects – changes in the magnetic field between the magnetosphere and the ionosphere which, by Faraday’s law, give a curl in the electric field (*Lockwood et al.*, 1990; *Lockwood and Cowley*, 1992; *Lockwood and Morley*, 2004). In steady-state, the electric field becomes curl-free and electrostatic potentials do map down magnetic field lines. In addition, in steady state the adiaroic boundaries are not moving. Steady state applies when data are averaged over a long enough timescale; however, theory of substorm growth and expansion predicts that it will not apply to the timescales of a few substorm cycles or less. That is not to say that balanced reconnection events, when dayside and nightside reconnection voltages are approximately equal, do not occur (*DeJong et al.*, 2008, *Lockwood et al.*, 2009): these can occur by chance but, probably more often, they occur because changes in the dayside reconnection voltage are sufficiently slow, such that it is never greatly different to the lagged nightside voltage response (*Milan et al.*, 2021). Surveys by *Lockwood et al.* (2009) and *Milan et al.* (2021) have looked at the relative occurrence of substorm cycles and quasi-balanced reconnection. Note that the ECPC model is the general case as it can predict quasi-steady, quasi-balanced reconnection (if the interplanetary conditions driving dayside reconnection vary slowly enough) as well substorm cycles. On the other hand, balanced reconnection is not the general case as it cannot predict substorm cycles (nor is there any known mechanism that can act to balance the reconnection rates at any one instant). *Lockwood* (1991) pointed out that the motion of adiaroic convection reversals boundaries means that they are smoothed out in average patterns of convection. On timescales shorter than the substorm cycle of polar cap expansion and contraction, ionospheric convection reflects both the DP-2 and DP-1 current systems and displays the

response delays associated with both (respectively a few minutes and 30-60 min). In addition, because of a combination of ionospheric incompressibility and the antisunward motion of open field lines, the response delay varies with location, increasing with distance away from noon (*Lockwood et al.*, 1986; *Saunders et al.*, 1992; *Lopez et al.*, 1999; *Morley and Lockwood*, 2005).

Convection is often quantified by the transpolar voltage  $\Phi_{PC}$  between convection reversal boundaries in the ionosphere on the dawnside and the duskside of the polar cap (*Reiff et al.*, 1981; *Cowley*, 1984; *Boyle*, 1997; *Hairston et al.*, 1998; *Liu et al.*, 2019). This parameter is measured by spacecraft in high-inclination, Low-Earth Orbit (LEO) by integration of the observed “along-track” component of the electric field along the satellite path between the two dominant Convection Reversal Boundaries (CRBs). That electric field can be either directly measured or derived from observations of the vector magnetic field,  $\vec{B}$  and the plasma flow  $\vec{V}$  and using the equation of ideal MHD  $\vec{E} = -\vec{V} \times \vec{B}$  which applies to a very high degree of accuracy even in the F-region ionosphere because of the high magnetic Reynold’s number (*Hanson et al.*, 1994). Hence by integrating the along-track electric field (corresponding to the cross-track drift) between the two main CRBs, the transpolar voltage  $\Phi_{PC}$  is measured for that satellite path. The quantity  $\Phi_{PC}$  is often accurately called the “polar cap potential drop”, but also frequently (but inaccurately) referred to as the “cross-cap potential” or “polar cap potential”. Strictly speaking, it is a potential difference, i.e., a voltage, and this semantic point has real physical significance to understanding because, by Faraday’s induction law, a voltage is synonymous with magnetic flux transfer rate whereas a potential is not. Hence, we here use the term “transpolar voltage” for  $\Phi_{PC}$  and note that it is the rate at which magnetic flux is transferred across the polar cap. One convention that can be used is that positive transpolar voltage means that the dawnside CRB potential exceeds the duskside CRB potential (i.e., the electric field is from dawn to dusk), and this applies most of the time because net flux transfer is from the dayside to nightside. The reason for this is that open flux is, by definition, embedded in the solar wind flow and the solar wind is always transferring that open flux antisunward and, during even the longest intervals of northward IMF, the open flux never decays away. This antisunward flux transport remains dominant during northward IMF despite interruptions by intervals of sunward flow of some open flux tubes caused by them being reconfigured by lobe reconnection taking place at the magnetopause at the sunward edge of the tail lobes (see review by *Lockwood and Moen*, 1999). In terms of

magnetospheric configuration and voltages, this means the geomagnetic tail is always present and so magnetic shear is always present between the two tail lobes giving some level of magnetic reconnection in the associated cross-tail current sheet. In addition, reconnection at the low-latitude dayside magnetopause (i.e., between the magnetic cusps) that opens geomagnetic field lines has been observed to continue (at a low level) during intervals of northward IMF (*Chandler et al.*, 1999; *Fuselier et al.*, 2000).

Figure 1 is a schematic of the three drivers of convection in the magnetosphere and ionosphere during southward IMF. This is adapted from *Cowley* (1982), but with the addition of a reconnection X-line in the cross-tail current sheet (in green, the voltage across which is  $\Phi_N$ ) that re-closes open field lines. This is included here because in the ECPC model (*Cowley and Lockwood*, 1992) it contributes to the ionospheric transpolar voltage  $\Phi_{PC}$ . The ECPC model predicts that at any one time, the effect of  $\Phi_N$  combines with the effect of the reconnection voltage  $\Phi_D$  along the dayside magnetopause reconnection X-line (in red) which generates open field lines. The third source of  $\Phi_{PC}$  illustrated here is “viscous-like” momentum transfer across the magnetopause onto closed field lines that generates a total antisunward magnetic flux transfer of closed flux of voltage  $\Phi_V$  in the low latitude boundary layers (LLBL) on the dawn and dusk flanks of the magnetosphere. Figure 2 is a schematic of ionospheric flow patterns that is compatible with Figure 1 and the ECPC model in general. Figure 2a shows the special case of steady-state ( $\Phi_D = \Phi_N$ ) with some viscous-like flow cells ( $\Phi_V > 0$ ) and is as in the schematic used by *Cowley* (1982). Figures 2b and 2c are examples of ECPC model predictions for, respectively, an expanding and a contracting polar cap. For polar cap expansion  $\Phi_D > \Phi_N$  and  $\Phi_{PC} \approx \Phi_D$ . For a contracting polar cap  $\Phi_N > \Phi_D$  and  $\Phi_{PC} \approx \Phi_N$ . In Figures 2b and 2c, no viscous flow excitation is included ( $\Phi_V = 0$ ), but several features often mistaken for viscous-like flows are seen in Figure 2c. In particular, the convection pattern shows flow streamlines entering the polar cap over the entire dayside and the transpolar voltage exceeds the dayside reconnection voltage ( $\Phi_{PC} \approx \Phi_N > \Phi_D$ ).

The presence of lobe stirring cells during northward IMF, or even lobe field line re-closure by reconnection at the sunward edges of both lobes (e.g. *Lockwood and Moen*, 1999), means that northward IMF is inherently a non-steady-state situation because, by Faraday’s law, the electric field has a curl with dawn-to-dusk electric field associated with reconnection in the cross-tail current sheet but dusk-to-dawn electric field along the lobe reconnection site(s) at

the sunward edge(s) of the lobe magnetopause (Lockwood, 2019). Hence during the 50% of time that the IMF points northward (Hapgood et al., 1991; Lockwood et al., 2017; 2019b) the magnetosphere is quiet but also inherently in a non-steady state because of the slow decay of open flux (see review by Lockwood, 2019).

Figure 3 gives two schematics of a northern hemisphere convection pattern that we would expect during northward IMF; specifically, if the IMF has (a) components  $B_Z > 0$  and  $B_Y = 0$  and (b)  $B_Z > 0$  and  $B_Y > 0$  in the GSM reference frame. Figure 3(a) shows the case of lobe reconnection (voltage  $\Phi_L$ ) driving symmetric lobe circulation cells in the open polar cap, as well as the effects of reconnection voltages  $\Phi_D$  and  $\Phi_N$  and a viscous-like voltage  $\Phi_V$ . In Figure 3(b), the magnetic curvature force on newly-reconfigured open field lines for the large positive IMF  $B_Y$  causes the dawn lobe cell to dominate: note in this case how the poleward contraction of the (dusk) adiaroic open polar cap boundary causes the sunward flowing portion at lower potentials of this one lobe convection cell to merge with the main dusk cell.

Because we here survey a very large dataset, we need to automate the scaling of transpolar voltage and we found that automated algorithms to distinguish and identify lobe cells from the cells driven by  $\Phi_D$ ,  $\Phi_N$  and  $\Phi_V$  were not reliable, particularly given that the merging of lobe and main flow cells illustrated in Figure 3b is often seen for northward IMF conditions. To enable automated scaling, we here define  $\Phi_{PC}$  by

$$\Phi_{PC} = \phi_{max} - \phi_{min} \quad (1).$$

We apply this, irrespective of the locations at which the maximum ( $\phi_{max}$ ) and minimum ( $\phi_{min}$ ) of the potential pattern occurs. This is good for investigating the ECPC model because it allows for the sunward and antisunward shifts of the locations of both  $\phi_{max}$  and  $\phi_{min}$  caused by dominant  $\Phi_D$  and  $\Phi_N$ , respectively (see Figures 2b and 2c). The maximum potential  $\phi_{max}$  is usually the potential at the centre of the main convention cell on the dawn flank of the polar cap ( $\phi_{dawn1}$  in Figure 3) and the  $\phi_{min}$  is usually the potential at the centre of the main cell on the dusk flank of the polar cap ( $\phi_{dusk1}$  in Figure 3). However, if the lobe reconnection voltage  $\Phi_L$  is large enough,  $\phi_{max}$  can become  $\phi_{dusk2}$  and/or  $\phi_{min}$  can become  $\phi_{dawn2}$ , where  $\phi_{dusk2}$  and  $\phi_{dawn2}$  appear across the ends of the footprint of the lobe reconnection X-line and are also defined in Figure 3. Hence if  $\phi_{dusk2} > \phi_{dawn1}$  and



216  $\phi_{dawn2} < \phi_{dusk1}$ , our definition means that  $\Phi_{PC} = \phi_{dusk2} - \phi_{dawn2} = \Phi_L$ . We will call  
 217  $\Phi_{PC}$  in this case a “lobe-dominated” value of  $\Phi_{PC}$ : note that it is a positive value even though  
 218 the dominant flow in the central polar cap is now sunward. If neither lobe cell sets  $\phi_{min}$  or  
 219  $\phi_{max}$  then  $\Phi_{PC}$  is the voltage associated with antisunward convection over the polar cap set  
 220 by  $\Phi_D$ ,  $\Phi_N$  and  $\Phi_V$ . We note below that this is the most common situation and hence we call  
 221 the resulting  $\Phi_{PC} = \phi_{dawn1} - \phi_{dusk1}$  a “conventional” value. There is a third possibility  
 222 where  $\phi_{dusk2} > \phi_{dawn1}$  or  $\phi_{dawn2} < \phi_{dusk1}$  but not both. In either of these two cases,  $\Phi_{PC}$   
 223 will be somewhat larger than the conventional value and we call this a “hybrid” value as  $\Phi_D$ ,  
 224  $\Phi_N$ ,  $\Phi_V$ , and  $\Phi_L$  can all contribute to  $\Phi_{PC}$ . *Wilder et al. (2008)* have surveyed SuperDARN  
 225 data and shown that the lobe reconnection voltage in the ionosphere  $\Phi_L$  saturates at about 15-  
 226 20 kV. This means that voltages above 20kV are almost all “conventional” values associated  
 227 with dominant antisunward transfer of flux over the polar cap and set by  $\Phi_D$ ,  $\Phi_N$  and  $\Phi_V$ .  
 228 However for  $\Phi_{PC} < 20\text{kV}$  we need to remain aware that  $\Phi_D$ ,  $\Phi_N$ ,  $\Phi_V$ , and  $\Phi_L$  can all  
 229 contribute to  $\Phi_{PC}$  for the hybrid cases and that for the lobe-dominated cases  $\Phi_{PC} = \Phi_L$ . For  
 230 our definition, the viscous-like voltage  $\Phi_V$  would only equal the  $\Phi_{PC}$  value if all three  
 231 reconnection voltages  $\Phi_D$ ,  $\Phi_N$  and  $\Phi_L$  were zero.

232 *Milan et al. (2021)* surveyed one-year of data and found that roughly 20% of all antisunward  
 233 magnetospheric flux transfer was during quiet periods, 43% during non-steady-state phases  
 234 (20.8% substorm growth, 9.8% substorm expansion, 3.3% substorm recovery, 1.2% recovery  
 235 bays and 8% multiple intensifications). The remaining 37% was during intervals they classed  
 236 as “driven” – these include extended substorm growth phases and periods when dayside and  
 237 nightside reconnection are close to being balanced ( $\Phi_D \approx \Phi_N$ ). This driven state was found  
 238 for 18.2% of the time, compared to 27.2% of the time for the non-steady phases. Together  
 239 these make up the 50% of time for which the IMF points southward and, as noted above,  
 240 northward IMF is inherently non-steady and so non-steady conditions are present 77.2% of  
 241 the time. Hence, in both time and resulting flux transfer, non-steady conditions are the  
 242 dominant magnetospheric response. However, we introduce steady state into our view of the  
 243 coupled magnetosphere-ionosphere system at all times if we average data together. In steady-  
 244 state, the rate of flux transfer across the polar cap,  $\Phi_{PC}$  equals the rate at which field lines are  
 245 opened by reconnection in the dayside magnetopause (the dayside reconnection voltage  $\Phi_D$ )  
 246 and the rate at which open field lines are closed by reconnection in the cross-tail current sheet

(the nightside reconnection voltage  $\Phi_N$ ), plus any non-reconnection “viscous-like” voltage,  $\Phi_V$  (i.e.  $\Phi_{PC} = \Phi_D + \Phi_V = \Phi_N + \Phi_V$ ). The balanced reconnection ( $\Phi_D \approx \Phi_N$ ) needed for steady state can occur at any one moment by chance or could be the result of a mechanism that maintains it. As yet, no such mechanism has been defined. Furthermore, there are reasons to believe that no such mechanism can be present: for it to operate, information about the magnetopause reconnection voltage at any one time  $\Phi_D$  would have to be able to reach the nightside reconnection site so the mechanism can modulate  $\Phi_N$ . Because of propagation delays, at the nightside reconnection site there can be no information about the instantaneous value of  $\Phi_D$  at the dayside reconnection site, and so  $\Phi_D \approx \Phi_N$  cannot happen as a matter of course, maintained by a balancing mechanism. Faraday’s law applied to the open-closed field line boundary gives the general behaviour:

$$dF_o/dt = B_i \cdot dA_o/dt = \Phi_D - \Phi_N \quad (2)$$

where  $F_o$  is the open magnetospheric flux,  $A_o$  the area of the open field line polar cap in the ionosphere and  $B_i$  is the magnitude of the field in the ionosphere (in this equation,  $B_i$  is assumed to be constant). Note that Equation (2) can be thought of as the continuity equation for the open flux  $F_o$ . Hence steady state requires  $\Phi_D = \Phi_N$  and  $dF_o/dt = dA_o/dt = 0$  and the fact that the polar cap area varies shows that non-steady conditions apply (*Holzer et al.*, 1986; *Milan et al.*, 2003; *Milan*, 2004). The results of *Lockwood et al.* (2009) and *Milan et al.* (2021) show that non-steady state is a common situation, which is to be expected because of the variability in the IMF orientation (and hence  $\Phi_D$ ) and the fact that the transfer of information from the dayside magnetopause reconnection site to that in the cross-tail current sheet takes time and hence  $\Phi_N$  can only respond after a lag. How common balanced convection ( $\Phi_D \approx \Phi_N$ ) events are found to be is a matter of definition (see *McWilliams et al.*, 2008) and they will be less common if tighter limits are placed on the maximum ( $\Phi_D - \Phi_N$ ) used to define them. For a large averaging timescale  $\tau$ , the time derivatives in equation (2) tend to zero because long-term trends in  $F_o$  and  $A_o$  are negligibly small. So, for large enough  $\tau$

$$\langle \Phi_{PC} \rangle_\tau - \langle \Phi_V \rangle_\tau = \langle \Phi_D \rangle_\tau = \langle \Phi_N \rangle_\tau \quad (3)$$

even though this condition only applies relatively rarely at any one instant of time during southward IMF.

The voltage  $\Phi_V$  is generated by any non-reconnection process transferring momentum from the flow of the shocked solar wind in the magnetosheath to closed field lines (e.g., *Farrugia et al.*, 2001). The ECPC model predicts that  $\Phi_V$  is small and that most of what had previously been thought to be voltage driven by viscous-like processes is, in fact, due to the nightside reconnection voltage  $\Phi_N$  which always persists because the geomagnetic tail never erodes away and so there is always magnetic shear in the centre of the tail (*Wygant et al.*, 1983, *Lockwood et al.*, 1990; *Lockwood*, 1991; *Milan*, 2004). Numerical simulations have confirmed that  $\Phi_N$  contributes to transpolar voltage  $\Phi_{PC}$  in addition to  $\Phi_D$  (e.g., *Gordeev et al.*, 2011).

*Lockwood* (1991) pointed out that a consequence of the ECPC pattern is that  $\Phi_{PC}$  for a given  $\Phi_D$ ,  $\Phi_N$  and  $\Phi_V$  will depend on the shape of the open polar cap and how it is changing and only for an open polar cap that remains circular at all times is the voltage across the centre of the polar cap equal to  $\Phi_V + (\Phi_D + \Phi_N)/2$ . Hence, in general, for the duration of each polar cap traversal by a LEO satellite we need to consider non-steady conditions, and that each  $\Phi_{PC}$  value observed will depend on  $\Phi_D$ ,  $\Phi_N$ , and  $\Phi_V$  and on how the polar cap is changing shape (i.e., the motion of the adiaroic boundaries which reflect the potential distribution along the boundary) and, critically, on the satellite path. Some changes in the polar cap shape are an integral part of the ECPC flow excitation mechanism proposed by *Cowley and Lockwood* (1992), specifically the equatorward expansion around noon caused by sudden increases in  $\Phi_D$  and the poleward contraction around midnight caused by sudden increases in  $\Phi_N$ . However, other polar cap shape distortions are likely. Examples include the effects of changes in the IMF  $B_Y$  component (*Lockwood*, 1991; *Cowley et al.*, 1991b) or transient and propagating filamentary field aligned currents in Travelling Convection Vortices induced by solar wind dynamic pressure pulses (e.g., *Lühr et al.*, 1996). In addition, prolonged northward IMF can lead to open flux collecting towards midnight, giving a more triangular open flux region characteristic of the “horse-collar” pattern in global auroral images (*Hones et al.*, 1989; *Birn et al.*, 1991): it has been proposed that this is enhanced by lobe reconnection taking place in both hemispheres which removes dayside open flux (*Milan et al.*, 2020). Hence the use of a circular open polar cap in Figures 2 and 3 is illustrative only. Nevertheless, in general, passes of the dayside polar cap will reflect the influence of  $\Phi_D$  to a greater extent and for passes over the nightside polar cap the influence of  $\Phi_N$  will be greater.

The question then arises as to what is the minimum averaging timescale  $\tau$  required to make equation (3) apply to a good approximation? Clearly,  $\tau$  smaller than about 3 hours is inadequate as it is comparable to the timescales of the substorm cycle over which the open polar cap expands and contracts (*Holzer et al.*, 1986; *Lockwood et al.*, 1990; *Lockwood and Cowley*, 1992, *Milan et al.*, 2003; 2009; 2012; *Huang et al.*, 2009). *Imber et al.* (2013) show that over the sunspot cycle the polar cap area is remarkably constant, making  $dF_o/dt$  negligible over timescales  $\tau$  of order years. Both modelling (e.g., *Lopez et al.*, 2001) and observational studies (e.g., *Mishin and Karavaev*, 2017) show that  $F_o$  rises during the initial phases of large geomagnetic storms but  $F_o$ , like  $\Phi_{PC}$  (e.g., *Kubota et al.*, 2017), appears to saturate establishing a temporary quasi-steady state, before falling again as the storm declines. These “Balanced Reconnection Intervals” (BRI) are related to the phenomenon of “Steady Magnetospheric Convection” (SMC) (*McWilliams et al.*, 2008) events but do not necessarily start with a substorm growth phase nor end with a substorm expansion phase (*DeJong et al.*, 2008); however, because in general there is a long-term variation in  $F_o$  around both BRI and SMC events (*Lockwood et al.*, 2009 ; *Milan et al.*, 2021) they cannot be considered a steady-state phenomenon on timescales shorter than their duration. However, we note that some BRI and SMC events probably can occur without prior, or subsequent, major change in  $F_o$  and these would be chance occurrences of matched  $\Phi_N$  and  $\Phi_D$  variations or because the rate of change in  $\Phi_D$  has been slow enough for  $\Phi_N$  to respond despite the propagation lag. Note also that the high variability of IMF orientation, and hence power input into the magnetosphere gives this a lower occurrence frequency than that non-steady conditions (*Lockwood et al.*, 2019b; c).

In general, we need  $\tau$  to exceed storm durations for steady state to fully apply. *Haines et al.* (2019) have surveyed geomagnetic storms in the homogeneous  $aa$  index,  $aa_H$  (*Lockwood et al.*, 2018a; b) since 1868, defining storms as when  $aa_H$  exceeded its overall 90<sup>th</sup> percentile: of the 10<sup>4</sup> storms defined by this threshold, none lasted more than 3 days. Hence  $\tau \geq 3$  days should generally make steady-state a valid assumption. We note that *Weigel* (2007) proposes that the time constant is considerably longer than this, such that non-steady conditions and solar wind history even means that the time of year influences the variation; however, as demonstrated by *Lockwood et al.* (2016), this would generate an “axial-like” time-of-day/time-of-year pattern and we can discount this proposal.

## 1-ii. SuperDARN Transpolar Voltage Data and Potential Patterns

The studies of transpolar voltage discussed in the previous section were made using observations of electric fields and plasma flows by LEO satellites as they passed over the polar caps. One problem with this is that the satellite path will not generally intersect the points of maximum and minimum potential and so the difference between them, the full transpolar voltage  $\Phi_{PC}$ , will be systematically underestimated. In addition, because there is no information of the potential pattern away from the satellite path, there is no way of checking if, or by how much, any one value is an underestimate. Studies have generally used passes that are close to the dawn-dusk meridian to try to minimise this problem, but the ECPC model predicts that this will only work for steady state conditions. This is because, as illustrated by Figures 2b and 2c, for dominant magnetopause reconnection ( $\Phi_D > \Phi_N$ ), both the maximum and minimum of the potential pattern will be shifted towards noon and for dominant tail reconnection ( $\Phi_N > \Phi_D$ ) they are shifted towards midnight. In this paper we use values derived from the SuperDARN (Super Dual Auroral Radar Network) coherent radar arrays (see review by *Chisham et al.*, 2007). By imaging the convection pattern, the points of maximum and minimum potential can be identified and the problem inherent in the spacecraft data avoided. As discussed in Section 1-i, we adopt the definition of  $\Phi_{PC}$  given in equation (1) and use an automated algorithm to compute it from patterns of the ionospheric potential,  $\phi$ .

However, there are some other important points to note about the transpolar voltage data from the SuperDARN radars. The radars monitor the line-of-sight component of the flow of F-region plasma by measuring the Doppler shift of coherent echoes that have reflected off convecting ionospheric irregularities embedded in the bulk plasma flow. The most accurate method for generating two-dimensional field-perpendicular convection velocity vectors from the SuperDARN radar data is by combining the line-of-sight measurements within a common field-of-view of pairs of radars (e.g., *Greenwald et al.*, 1995). However, because of the aspect sensitivity of echoes with respect to the structures causing the scatter, for much of the time when echoes are recorded by one radar, they are not detected by the twin radar looking in a different direction and so opportunities to make these “bistatic” observations are relatively rare. Hence methods to find the functional form for the distribution of electrostatic potential  $\phi$  that was a best fit to all the line-of-sight velocity measurements were developed (*Ruohoniemi*

and Baker, 1998; Cousins *et al.*, 2013). The most widely used of these is the “map-potential” technique (a form of re-analysis using data-assimilation), which performed well when tested against available bistatic vectors (Provan *et al.*, 2002). However, lack of radar coverage and/or of the required scattering irregularities mean that line-of-sight data are not available at all locations in the polar regions and so the velocity data are supplemented with predictions by a statistical model, driven by the IMF conditions observed by an upstream monitor. From each derived map-potential pattern the transpolar voltage  $\Phi_{PC}$  can be scaled (Bristow *et al.*, 2004; Wilder *et al.*, 2011). A review of the development and application of this technique has been presented by Chisham *et al.* (2007).

The statistical model predictions used in the map-potential technique are weighted to minimize their impact for a given number of available radar echoes,  $n_e$  (Shepherd and Ruohoniemi, 2000). At times there are sufficient numbers and wide enough spatial distribution of echoes for the potential pattern to be determined from the radar data alone; on the other hand, in extreme cases with no echoes ( $n_e = 0$ ), the pattern is determined purely by the model and hence by the observed upstream interplanetary conditions. Tests of flow velocities derived using the SuperDARN radars have been made by comparing the map-potential flow estimates with data from the Defense Meteorological Satellite Program, DMSP (e.g., Xu *et al.*, 2007a; b; Drayton *et al.*, 2005) and Swarm (Koustov *et al.*, 2019a) spacecraft. In addition, transpolar voltage data from the SuperDARN map-potential data have been compared to those derived by the AMIE (Assimilative Mapping of Ionospheric Electrodynamics) technique that uses a variety of sources, particularly magnetometers (Gao, 2012). Given that there is a tendency for flow speeds defined by SuperDARN to be about 30% lower than seen by satellites (Xu *et al.*, 2007b; Drayton *et al.*, 2005; Koustov *et al.*, 2019a), but that convection reversal boundary locations in the two data sets are very similar, we would expect SuperDARN values of  $\Phi_{PC}$  to be well correlated with the satellite values but typically 30% lower. From the detailed comparison shown in part (c) of Figure A1 in Appendix A, allowing for the effect of the number of data echoes  $n_e$  and the proximity of the satellite pass, we find a similar result but the best fit regressions (linear and non-linear) show that the radar values are typically 20% lower.

In this paper we use a variety of threshold values  $n_{min}$  of the number of radar echoes  $n_e$  to investigate the effect of low  $n_e$  on our results. All  $\Phi_{PC}$  values based on  $n_e < n_{min}$  echoes

were discarded, and we varied  $n_{min}$  to determine the sensitivity of our results to the choice of  $n_{min}$ .

The use of a  $n_e > n_{min}$  selection criterion has an important but subtle implication for biases in the data because considerably fewer echoes are received during summer. This is probably due to combination of causes acting together including: sporadic E-blanketing of F-region radar returns; interference from enhanced ground echoes; a smoother ionosphere when photoionization rate is high and the effects of radar transmitter frequency selection (*Koustov et al.*, 2019b and references therein). Here, we only use potential maps from the northern hemisphere radar array with its greater number of stations and the means of  $n_e$  are consistently about 200 around the June solstice (summer) whereas they are typically between 500 and 600 around the December (solstice) winter. This means that hourly values that meet, for example, a  $n_e > n_{min} = 255$  criterion are quite rare in summer and atypical (around 2-3 per day, whereas there are typically 20-24 per day in winter).

The other factor that we need to be aware of is that the occurrence of echoes also increases with the plasma velocity (*Koustov et al.*, 2019b). This means that although we want to avoid samples with low  $n_e$  to minimise the role that the data-assimilation statistical convection model plays in the  $\Phi_{PC}$  value, we do not want to eliminate too many samples because that would preferentially remove low-flow (and hence low- $\Phi_{PC}$ ) samples.

The ECPC model has been used quantitatively to match to map-potential SuperDARN observations of the evolution of the convection pattern and  $\Phi_{PC}$  following individual events of southward and northward turnings of the IMF (*Lockwood et al.*, 2006), events that were also quantitatively compared with the associated signatures of magnetopause reconnection in cusp proton precipitation and aurora (*Lockwood et al.*, 2003; *Throp et al.*, 2005). Here we make a statistical study of the  $\Phi_{PC}$  data from SuperDARN using data from 25 years – more than a full Hale solar magnetic cycle.

## 2. Data Employed

In this paper we make use of 214410 hourly observations of the ionospheric transpolar voltage  $\Phi_{PC}$ , as defined by equation (1), derived from map-potential  $\phi$  patterns obtained by the northern-hemisphere SuperDARN radar network between 1995 and 2020. These data are

generated by applying the map-potential technique to data from 2-minute integration periods and the 30 values of  $\Phi_{PC}$  and  $n_e$  in each hour were then averaged together. The processed data have been checked using comparisons with dawn dusk passes by DMSP satellites from 2001-2002 for which the SuperDARN convection patterns show potential minima and maxima close to the satellite path (see Appendix A).

We compare with data on the north-south component of the IMF in the GSM frame,  $B_Z$  (defined positive northward), and the solar wind dynamic pressure,  $p_{SW}$ , both taken from the OMNI dataset, compiled and maintained by NASA's Goddard Space Flight Center (*King and Papitashvili, 2005*). We also compare with the  $AL$  auroral electrojet geomagnetic index compiled and maintained by the World Data Centre for Geomagnetism, Kyoto. We use one-minute values of  $B_Z$ ,  $p_{SW}$  and  $AL$ . Because we are not sure of the precise propagation lags of these parameters relative to the  $\Phi_{PC}$  data we take running (boxcar) means over a timescale  $\tau$  which we then interpolate to the mid-point of the hour over which  $\Phi_{PC}$  data are averaged, minus a nominal lag  $\delta t$ . We repeated all studies using two values of  $\tau$ ,  $\tau = 1 \text{ hr}$  to match the averaging timescale of the  $\Phi_{PC}$  data and  $\tau = 15 \text{ min.}$ : plots for the two were almost identical and we use  $\tau = 15 \text{ min.}$  in the plots shown. For IMF  $B_Z$  we use a lag  $\delta t = 5 \text{ min.}$ , to allow for propagation across the magnetosheath to the dayside magnetopause reconnection X-line and then down geomagnetic field lines to the ionosphere, because we are interested in the effect of IMF  $B_Z$  on the dayside reconnection voltage  $\Phi_D$ . For  $p_{SW}$  we have tried two different values of  $\delta t$ : to search for an effect of  $p_{SW}$  on  $\Phi_D$  we use  $\delta t = 5 \text{ min}$  as for IMF  $B_Z$ , and to search for an effect of  $p_{SW}$  on  $\Phi_N$  we use  $\delta t = 75 \text{ min}$  (derived below). The latter effect is expected from squeezing of the near-Earth tail, as recently observed and modelled by *Lockwood et al. (2020a; b; 2021)*. Because of the persistence (i.e., a high and broad autocorrelation function) in the  $p_{SW}$  data series, the results are similar for the two  $\delta t$  values; however, slightly clearer effects are seen for  $\delta t = 75 \text{ min.}$  and that is the value employed in the plots presented here. For  $AL$ , we use  $\delta t = 0$  as both  $AL$  and the  $\Phi_N$  value are used as an indicator of signatures in the nightside auroral ionosphere. We compute  $p_{SW} = m_{SW} N_{SW} V_{SW}^2$  from 1-minute values of the solar wind mean ion mass  $m_{SW}$ , number density  $N_{SW}$  and speed  $V_{SW}$ ; in the case of  $m_{SW}$  these are linearly interpolated from 5 min., 15 min or hourly observations if 1-min. values are unavailable.



We note that a great many papers derive propagation delays  $\delta t$  between solar wind features and responses in the magnetosphere and ionosphere. These are not always comparable because different solar wind features and different responses are considered. In addition, some effects call for IMF orientation to be considered whereas others do not. In addition, the solar wind speed varies and alters the  $\delta t$  values. Some studies use correlations to define the peak response whereas other use the timing of the first detectable response. A detailed and extensive statistical study of the delay between changes in the IMF  $B_y$  component and their effect appearing in the near-Earth tail lobes and plasma sheet was presented by *Browett et al.* (2017). They found optimum delays of 1 hr for southward IMF but up to 5 hr for northward IMF conditions. Because these are the times for the magnetic curvature force to take effect in the tail, they relate to field-aligned Alfvén wave propagation times as well as solar wind propagation times and so are not directly comparable with, for example, the propagation time for dynamic pressure change effects in the tail. We note that the value of  $\delta t = 75 \text{ min}$  that we here derive and use, is slightly longer than the 60 min that *Browett et al.* (2017) derive for southward IMF but much shorter than 300 min that they find sometimes derived for northward IMF.

### 3. Results

#### 3-i. Effect of number of radar echoes, $n_e$

Figure 4 shows the cumulative probability distribution (c.d.f.) of the number of radar echoes  $n_e$  for the 214410 samples of the ionospheric transpolar voltage,  $\Phi_{PC}$ . The vertical coloured lines show a set of nominal values of  $n_{min}$ , which we vary from 100 (dark red) to 900 (mauve) in steps of 100 in our sensitivity study (i.e.,  $n_{min} = [100:100:900]$ ). These values yield subsets of 137633, 85078, 52501, 32646, 20378, 12866, 8032, 4958, and 3134 samples. The black dashed line is for  $n_{min} = 255$  which we discuss below, and which yields 60653 samples, very close to 30% of the original dataset.

Figure 5 shows the probability distribution functions for hourly transpolar voltage,  $\Phi_{PC}$ , selected using the condition  $n_e > n_{min}$  for the values of  $n_{min}$  used in Figure 4. It can be seen that the shape of the distribution varies with  $n_{min}$ , the mode value of the normalised distribution getting smaller and moving to higher values. The large-value tail of the

distribution therefore gets relatively larger, as expected from the discussion in section 1-ii. It can be seen that for  $n_{min} < 300$  the effect on the distribution shape is, however, relatively minor.

To further define an optimum value for  $n_{min}$  we have carried out a comparison with dawn-dusk passes by DMSP satellites for the years 2001 and 2002 and compared the transpolar voltage derived,  $[\Phi_{PC}]_{DMSP}$ , with the simultaneous SuperDARN map-potential estimates,  $[\Phi_{PC}]_{S.DARN}$ . We computed the root mean square deviation,  $(\langle \Delta\Phi_{PC}^2 \rangle)^{1/2}$  (where  $\Delta\Phi_{PC} = [\Phi_{PC}]_{DMSP} - [\Phi_{PC}]_{S.DARN}$ ) as a metric of agreement. In general, we found  $\Delta\Phi_{PC}$  tended to be positive, consistent with the studies discussed in section 1-ii. We used the Nelder-Mead search to find a minimum in  $(\langle \Delta\Phi_{PC}^2 \rangle)^{1/2}$  as a function of  $n_{min}$  and the maximum allowed geocentric angular separation of the satellite and radar potential maxima and minima,  $\delta$ . This yielded an optimum  $n_{min}$  of 255 and for the optimum maximum  $\delta$  of  $30^\circ$ . The use of  $n_{min} = 255$  gave a peak correlation between  $[\Phi_{PC}]_{DMSP}$  and  $[\Phi_{PC}]_{S.DARN}$  of 0.85 with an r.m.s. deviation  $(\langle \Delta\Phi_{PC}^2 \rangle)^{1/2} = 18.5 \text{ kV}$ , compared to a correlation of 0.82 for  $n_{min} = 0$ , for which  $(\langle \Delta\Phi_{PC}^2 \rangle)^{1/2} = 21.2 \text{ kV}$  (see Appendix A). Hence agreement was most improved by adopting of  $n_{min} = 255$  which is a value small enough not to greatly change the shape of the overall distribution of  $[\Phi_{PC}]_{S.DARN}$  values, as shown by Figure 5. We also used this survey to calibrate the SuperDARN estimates: where comparisons are made, we here correct the systematically higher values (by a factor of 20%) from the satellite observations using the linear regression of the  $[\Phi_{PC}]_{DMSP}$  and  $[\Phi_{PC}]_{S.DARN}$  data for  $n_{min} = 255$  and  $\delta < 30^\circ$  (see Appendix A).

In sections 3-ii to 3-iv of this paper we employ the selection criterion  $n_e > n_{min} = 255$  (which gives us 60653 samples). However, in section 3-v we return to using all the  $n_{min}$  values used in Figures 4 and 5 in a sensitivity study to show that our conclusions are not influenced by the value of  $n_{min}$  adopted.

### 3-ii. Variation of $\Phi_{PC}$ with IMF $B_Z$ and the $AL$ index

Figure 6 analyses the optimum propagation lags needed for this study. The black line is the lag correlogram (linear correlation coefficient as a function of lag) for  $\Phi_{PC}$  and the IMF  $-B_Z$  value (in the GSM frame). The peak correlation is with  $\Phi_{PC}$  lagging behind  $B_Z$  by  $\delta t = 20$

517 min. This is longer than the response time for dayside magnetopause reconnection (*Etemadi*  
 518 *et al.*, 1988; *Todd et al.*, 1988): from the propagation delay to cross the magnetosheath, this is  
 519 expected to be about 5 min. which is the typical response time seen in the observational  
 520 studies discussed in section 1-i. The propagation of the enhancement to the centre of the  
 521 polar cap was modelled using the ECPC model by *Morley and Lockwood* (2005) and a value  
 522 of 20 minutes from the nose of the bow shock is broadly consistent with their predictions.  
 523 Figure 2b shows that if the nightside reconnection voltage  $\Phi_N$  is small, the transpolar voltage  
 524  $\Phi_{PC}$  is approximately equal to  $\Phi_D$  and if we also fold in a non-zero viscous voltage this  
 525 becomes  $\Phi_{PC} \approx \Phi_D + \Phi_V$ . In addition, Figure 2b shows that this voltage appears between  
 526 maximum and minimum potentials at points that are close to the ends of the ionospheric  
 527 footprint of the magnetopause reconnection X-line. In this case the response of  $\Phi_{PC}$  to IMF  
 528  $B_z$  would be after the short lag with which  $\Phi_D$  responds (i.e.,  $\delta t \approx 5 \text{ min}$ ). The  $AL$  index is  
 529 expected to be a good proxy for the nightside voltage  $\Phi_N$ , becoming more negative as  $\Phi_N$   
 530 increases. Hence a subset of the data selected for a small  $-AL$  should be give  $\Phi_{PC}$  values  
 531 dominated by  $\Phi_D$  and hence showing a small response lag. For the subset of data when the  $AL$   
 532 index is above 100 nT (i.e.,  $-AL < 100 \text{ nT}$ ), shown by the blue line in Figure 6, the observed  
 533 lag of  $\Phi_{PC}$  lag after  $B_z$  of  $\delta t = 5 \text{ min}$  is therefore consistent with the ECPC model and low  
 534  $\Phi_N$ . A notable feature of all the correlograms in Figure 6, except those for  $\Phi_{PC}$  and  $B_z$  (in  
 535 blue and black), is that the peaks are asymmetric with higher correlations at a given time after  
 536 the peak than for the same time before it. This shows that higher auroral activity (i.e., larger  
 537 negative  $AL$ ) are responses over longer time constants and that time constant is variable.  
 538 The orange line shows that the optimum lag for the  $AL$  index after  $B_z$  is  $\delta t = 35 \text{ min}$ , but the  
 539 peak is lower and broader indicating there is considerable variability in that lag. The green  
 540 line gives the lag of the  $AL$  index after  $\Phi_{PC}$  of  $\delta t = 25 \text{ min}$ , which yields a total lag of  $25+20$   
 541  $= 45 \text{ min}$  after IMF  $B_z$  which is 10 min longer than the value obtained from the direct  
 542 correlation between  $AL$  and IMF  $B_z$ . The mauve line shows the correlation between  $\Phi_{PC}$  and  
 543 solar wind dynamic pressure  $p_{SW}$  which is considerably weaker than the other correlations, as  
 544 expected because  $\Phi_{PC}$  depends primarily on  $\Phi_D$  and  $\Phi_N$  which are not expected to be as  
 545 strongly modulated by  $p_{SW}$  as they are by  $B_z$ . However, this  $\Phi_{PC}$  versus  $p_{SW}$  correlogram  
 546 does show a broad, weak peak with a maximum at a lag of  $\delta t = 120 \text{ min}$ . This suggests that  
 547 if  $p_{SW}$  is exerting an influence on  $\Phi_{PC}$  it is mainly via a modulation of  $\Phi_N$  through squeezing  
 548 the near-Earth cross-trail current sheet. This will be discussed further in section 3-iii. The

correlation between  $\Phi_{PC}$  and  $p_{SW}$  was also examined for northward and southward IMF conditions separately by selecting data when the  $B_z$  data simultaneous with  $p_{SW}$  was positive and negative, giving the cyan and grey correlograms, respectively. For southward IMF, the peak effect is soon after that of the peak response to IMF  $B_z$  and so this appears to show an influence of  $p_{SW}$  on the dayside reconnection voltage  $\Phi_D$ . On the other hand, the peak response for northward IMF is at a lag of  $\delta t = 75 \text{ min.}$  and because of the absence of large  $\Phi_D$  in these cases, this appears to show a response of  $\Phi_N$  to increased  $p_{SW}$  in these cases (see discussion by *Lockwood, 2013*). In our studies we used  $\delta t$  of 5, 75 and 120 min. for the optimum lag between  $p_{SW}$  and terrestrial responses: because of the high persistence in the  $p_{SW}$  data series the results were very similar in the three cases, and we here show values for  $\delta t = 75 \text{ min.}$

A great many studies have presented scatter plots of  $\Phi_{PC}$  as a function IMF  $B_z$  (or dawn-dusk interplanetary electric field  $V_{SW}B_z$ , but the radial solar wind speed  $V_{SW}$  explains very little of the scatter) and shown that  $\Phi_{PC}$  increases approximately linearly with  $-B_z$  for  $B_z < 0$  but has approximately constant and small values for  $B_z > 0$ . Figure 7a shows that the SuperDARN dataset used here also confirms this behaviour by comparing a scatter plot of the  $\Phi_{PC}$  values as a function of IMF  $B_z$  (black points) with the corresponding scatter plot from the survey by *Cowley (1984)* using data from a variety of LEO spacecraft (mauve points). Note that the satellite  $\Phi_{PC}$  values have been reduced by the 20% factor found from comparisons with two years' passes by the DMSP satellites (see Appendix A). Because there are so many samples in our study, a scatter plot loses a great deal of information because so many points are plotted on top of each other. Hence in Figure 7b we color-code the fraction of samples ( $n/\Sigma n$ , on a logarithmic scale) in bins of narrow width in both  $\Phi_{PC}$  and  $B_z$ . The bins used are  $\Delta B_z = 0.5 nT$  wide in IMF  $B_z$  and  $\Delta \Phi_{PC} = 2 \text{ kV}$  wide in the  $\Phi_{PC}$ . The plot shows the features that are familiar from other plots. Two important features to note are that: (1) for southward IMF there is a considerable spread in  $\Phi_{PC}$  at a given  $B_z$ ; and (2) for northward IMF that spread decreases with increasingly positive  $B_z$ . The plot also shows that  $\Phi_{PC}$  values increase slightly with increasingly positive  $B_z$  which implies that the lobe reconnection voltage  $\Phi_L$  increasingly becomes a factor, as discussed in relation to Figure 3. In the ECPC model, the spread at a given IMF  $B_z$  is expected because in non-steady state both  $\Phi_D$  and  $\Phi_N$  contribute to  $\Phi_{PC}$ . From long-term averages (for which  $\Phi_{PC} = \Phi_D + \Phi_V$ )

we know that  $(\Phi_D + \Phi_V)$  varies approximately linearly with  $-B_z$  for  $B_z < 0$ . It is also known that the auroral electrojet indices  $AE$  and  $AL$  vary approximately linearly with  $\Phi_{PC}$ , again with considerable scatter (Weimer *et al.*, 1990). In this paper we investigate the nightside auroral electrojet index  $AL$  as a proxy for the nightside voltage,  $\Phi_N$ , which is consistent with its use as a substorm expansion phase identifier in substorm cycles. Lockwood *et al.* (2009) used satellite passes to show that, statistically, polar cap flux decayed (i.e.,  $\Phi_N$  is enhanced) during substorm expansion phases when  $-AL$  is enhanced. Hubert *et al.* (2006) and Milan *et al.* (2009) used auroral images to also infer the loss of open flux during substorm expansion phases which also implies a relationship between  $-AL$  and  $\Phi_N$ . The variation of  $\Phi_N$  inferred from time-constants by Laundal (2020) shows a strong variation with  $-AL$ , as does the analysis of the polar cap boundary location by Aikio *et al.* (2013).

Figure 7c shows the mean  $AL$  values in the same bins as used in Figure 7b and Figure 7d shows contours of these mean  $AL$  data. Note that these contours can only be fitted in areas where the data are not sparse (identified by Figure 7b). It can be seen that the spread in  $\Phi_{PC}$  at a constant  $B_z$  is indeed associated with the spread in  $AL$ , as predicted by the ECPC model.

Figure 8a plots the variation of the occurrence of combinations of the  $AL$  index and IMF  $B_z$  using the same bins in  $B_z$  as used in Figure 7b and 7c and bins of  $AL$  that are 10 nT wide. Figure 8b shows the mean  $\Phi_{PC}$  in the same bins as used in Figure 8a and Figure 8c shows the fitted contours of mean  $\Phi_{PC}$  from the same data. The tilt of the contours towards the diagonal in 8b and 8c shows clearly that  $\Phi_{PC}$  depends on both  $B_z$  and  $AL$ : at constant  $AL$ ,  $\Phi_{PC}$  increases with increasingly negative  $B_z$  (moving horizontally to the left of the plot) but importantly,  $\Phi_{PC}$  also increases with increasingly negative  $AL$  at constant  $B_z$  for  $B_z < 0$  (moving vertically up the left-hand half of the plot). Hence  $\Phi_{PC}$  increases with increases in both IMF  $-B_z$  and  $-AL$ .

### **3-iii. Evolution of $\Phi_{PC}$ during northward IMF with time since the IMF turned northward**

A second scatter plot that was important verification of the ECPC model was presented in Figure 6 of Wygant *et al.* (1983). The plot looked at  $\Phi_{PC}$  values during northward IMF, as a function of time  $\Delta t$  since the IMF last had a southward component. Shortly after a northward turning (small  $\Delta t$ ), Wygant *et al.* found that almost the same range in  $\Phi_{PC}$  was present as had

been seen during the prior periods of southward IMF. However, with increased time after the northward turning (larger  $\Delta t$ ) this range decreased because the largest observed  $\Phi_{PC}$  declined exponentially. This decline continued until after about 10 hours only low values of  $\Phi_{PC}$  were seen. This behaviour is uniquely explained by the ECPC model which predicts that the larger values of  $\Phi_{PC}$  seen when the IMF is northward are because there is a large  $\Phi_N$  (despite  $\Phi_D$  being small because the IMF was northward). Large  $\Phi_N$  can still be present because of the large open flux that had been produced in the growth phase prior to the northward turning of the IMF, there being a delay before that flux is fully appended to the near-tail tail lobes by the solar wind flow. The inference was that the longer the IMF remained northward, the more events of higher  $\Phi_N$  had depleted the open flux and so the maximum of subsequent events was reduced.

The Wygant *et al.* plot contained only 28 datapoints, it is here reproduced in Figure 9a for the 29373 datapoints available from our survey for IMF  $B_z > 0$  and  $n_e > 255$ . To evaluate the time since the IMF had a southward component, we here use 6-minute boxcar running means of IMF  $B_z$  to avoid periods of northward IMF being interrupted by just a brief interval of southward IMF. For each northward-IMF  $\Phi_{PC}$  value observed at time  $t_o$  we evaluate the time at which the IMF turned northward in these 6-minute running means,  $t_n$ , and hence  $\Delta t = t_o - t_n$ . We did also try using running means over 15 minutes and 60 minutes and Figure 9 was not substantially changed other than the appropriate resolution in  $\Delta t$  was lowered. Again, because of the large number of samples, we colour code the fraction of samples  $n/\Sigma n$  (on a logarithmic scale) and all panels of Figure 9 uses bins in  $\Phi_{PC}$  that are 2 kV wide (as in Figures 7 and 8) and in  $\Delta t$  that are 6 min wide. The near-exponential decay of the largest  $\Phi_{PC}$  found by Wygant *et al.* is clear in Figure 9a and the time constant for that decay is very similar, with  $\Phi_{PC}$  reduced to almost constant value by  $\Delta t = 15$  hrs. The ECPC model predicts that the larger  $\Phi_{PC}$  values at a given  $\Delta t$  will be due to larger  $\Phi_N$  and hence greater  $-AL$ . Figure 9b confirms that this is indeed the case by color-coding the mean of  $-AL$  in the same bins as used in Figure 9a. Wilder *et al.* (2008) have used SuperDARN data to show that the lobe reconnection voltage in the ionosphere saturates at about 15-20 kV. From this we deduce that the voltages shown in Figures 9 for  $\Delta t$  greater than about 15 hours after the IMF turned northward are consistent with the effects of lobe reconnection. On the other hand, the values above 20 kV at  $\Delta t$  below about 10 hours (when  $AL$  is also enhanced) are not and we attribute these to enhanced  $\Phi_N$ .

Because we are belatedly reproducing the highly significant plot by *Wygant et al.* (1983), it is worth making a direct comparison. This is done as two superposed scatter plots of  $\Phi_{PC}$  as a function of time since the IMF was last southward  $\Delta t$  in the top panel of Figure 10. The black dots are from the present survey, the mauve dots the data of *Wygant et al.* (1983). As in Figure 7, the satellite  $\Phi_{PC}$  values have been reduced by the 20% found in the comparison in Figure A1c of Appendix A. It can be seen that the trend inferred by *Wygant et al.* from their small data set is confirmed in our large survey. The lower panel shows the contours of mean  $-AL$  in our survey and confirms the role of nightside reconnection invoked by the ECPC model explanation of the *Wygant et al.* plot.

### 3-iv. Effect of solar wind dynamic pressure, $p_{SW}$

In this section we investigate the effect of solar wind dynamic pressure  $p_{SW}$  on the tail of the magnetosphere. From Figure 6, we use  $p_{SW}$  values taken  $\delta t = 75 \text{ min}$  before the corresponding  $AL$  and  $\Phi_{PC}$  observation to allow for a propagation lag  $\delta t$  through the magnetosheath from the nose of the magnetosphere to sufficient distances down the tail to squeeze the tail reconnection site and so modulate the tail reconnection voltage  $\Phi_N$ . The analysis was also carried out for  $\delta t = 5 \text{ min}$  appropriate for the propagation from the nose of the magnetosphere to the dayside magnetopause and  $\delta t = 120 \text{ min}$  that gives the peak correlation between  $p_{SW}$  and  $\Phi_{PC}$ . The autocorrelation function of  $p_{SW}$  only falls to 0.5 at a lag of 6 hours and because of this great persistence in the  $p_{SW}$  data series, essentially the same features as shown here were observed for all three  $\delta t$  values used.

Figure 11 looks at the dependence on IMF  $B_z$  and the solar wind dynamic pressure (normalised by the mean, i.e.,  $p_{SW}/\langle p_{SW} \rangle$ ) of (top) the mid-latitude  $am$  geomagnetic range index, (middle) the mean  $-AL$  and (bottom) the mean transpolar voltage  $\Phi_{PC}$ . In the left-hand panels averages are given in bins that are  $\Delta B_z = 0.5 \text{ nT}$  wide in IMF  $B_z$  and 0.1 wide in  $p_{SW}/\langle p_{SW} \rangle$ . The right-hand panels show fitted contours to these data and highlight the gradients (but unlike the mean values contours cannot be plotted in areas where the data are sparse). For all panels, values increase as we move to the left, i.e., with increasingly southward IMF. This is seen at all  $p_{SW}/\langle p_{SW} \rangle$  values. All parameters show an increase with  $p_{SW}/\langle p_{SW} \rangle$ , at a given IMF  $B_z$  for  $B_z > 0$  and for all three parameters this increase decreases as the IMF becomes increasingly southward (i.e., the tilted contours become progressively more vertical). For the  $am$  index we see clear increases with increasing  $p_{SW}$  at

all IMF  $B_z$ , although they are weaker for more strongly southward IMF. This effect of  $p_{SW}$  on  $am$  has recently been identified and modelled by *Lockwood et al.* (2020a; b; 2021) as being the effect of  $p_{SW}$  in squeezing the near-Earth tail. For both  $-AL$  and  $\Phi_{PC}$ , on the other hand the contours become vertical for strongly southward IMF and the effect of enhanced  $p_{SW}$  is no longer present. We infer  $AL$  and  $\Phi_{PC}$  respond to increased  $\Phi_N$  caused by the squeezing effect of  $p_{SW}$  on the magnetic shear across near-Earth cross tail current sheet, for northward IMF and for weakly southward IMF. From the studies of *Lockwood et al.* (2020a; b; 2021) we believe  $am$  also responds to the enhanced energy density stored in the tail lobes because of the same squeezing effect of  $p_{SW}$ . Figure 12 confirms the trends to higher values at higher  $p_{SW}$  by showing the mean values, averaged over all IMF  $B_z$ , with error bars of plus and minus one standard deviation: these are large because of the large variation introduced by  $B_z$ . The upward trend is seen in all three parameters but noticeably the gradient of the third-order polynomial fit decreases at larger  $p_{SW}$  for both  $AL$  and  $\Phi_{PC}$ . The grey areas in Figure 12 are bounded by plus and minus 1-sigma error in the polynomial fit.

Figure 9c shows that the  $p_{SW}$  effect does play a role in the behaviour during northward IMF. This plot is the same as 9a and 9b but shows the mean values of  $p_{SW}$  in the bins. It can be seen that the larger values of  $\Phi_{PC}$  at a given time since the IMF turned northward tend to be at larger  $p_{SW}$ .

### 3-v. A sensitivity study of the effects of the availability of radar echoes

In the above sub-sections, all the plots shown are for the number of radar echoes  $n_e > n_{min} = 255$ . We have also generated all the plots using all of the 9  $n_{min}$  values given by the coloured lines in Figure 4. The trends in all plots are the same, the main effect being to change the absolute values in the means of  $\Phi_{PC}$ . Figure 13 compares the variations of  $\Phi_{PC}$  with IMF  $B_z$  for the thresholds  $n_{min}$  of [100:100:900] (i.e., between 100 and 900 in steps of 100), shown in Figure 13b with that for  $n_{min} = 255$  shown in Figure 13a. In Figure 13a the mean values and standard deviations are given for each  $B_z$  bin as well as the 6<sup>th</sup>-order polynomial fit (solid line). In Figure 13b only the polynomial fits are plotted to avoid overplotting the multiple cases. It can be seen that the same behaviour is seen at all  $n_{min}$  values, the main difference being that  $\Phi_{PC}$  values are systematically higher for larger  $n_{min}$  at all values of IMF  $B_z$ . This is expected because removal of values based on low numbers of



echoes systematically removes low  $\Phi_{PC}$  samples, as shown by Figure 5. We note that this effect is seen for both northward and southward IMF samples, except for the very largest (positive)  $B_Z$  when the mean  $\Phi_{PC}$  is close to 25 kV, irrespective of the  $n_{min}$  used.

Figure 14 makes the equivalent comparisons of the average variations of  $\Phi_{PC}$  for  $B_Z > 0$  with time elapsed  $\Delta t$  since the IMF turned northward. Again the clear trend is to larger  $\Phi_{PC}$  at larger  $n_{min}$ . However, this is not true at all  $\Delta t$  as the effect declines in amplitude at  $\Delta t > 5hrs$  and is not seen at all at  $\Delta t > 10hrs$ , such that at the largest positive  $B_Z$  all  $n_{min}$  thresholds give a near constant  $\Phi_{PC}$  of 15 kV.

We emphasise that all the plots presented in the Sections 3-ii, 3-iii and 3-iv have been generated using all 9  $n_{min}$  thresholds of  $n_e$  used in Figures 4, 5, 13 and 14. In every case the form of the plot is essentially the same, the main effect being that there are fewer samples available and so the plots cover smaller ranges of the parameters as noise due to lack of samples becomes a greater issue in the tails of the distributions.

## **4. Discussion and conclusions**

### **4-i. The dependence of transpolar voltage on magnetic reconnection in both the magnetopause and the cross-tail current sheet**

We have regenerated two scatter plots that formed an important basis for the space physics community's understanding of magnetospheric and ionospheric convection. The plots of transpolar voltage as a function of the IMF  $B_Z$  (for example, by *Reiff et al.*, 1981; *Cowley*, 1984; *Boyle*, 1997; *Hairston et al.*, 1998) were generated using typically less than 100 satellite passes. The plot by *Wygant et al.* (1983) of transpolar voltage as a function of time since the IMF was last southward was generated from just 28 data points. We here increase those numbers of data points by factors of over 1000 using convection patterns derived from the SuperDARN array of ground-based coherent radars.

We have used the *AL* auroral electrojet index to show that the scatter in these plots is well explained by the effect of the nightside voltage caused by reconnection in the cross-tail current sheet, as predicted by the Expanding-Contracting Polar Cap (ECPC) model (*Cowley and Lockwood*, 1992), and as was postulated in discussion and application of the model (e.g.,

*Lockwood and Cowley, 1992; Milan, 2004; Lockwood and Morley, 2004; Lockwood et al., 2006; Milan et al., 2003; 2021*). This has not been illustrated as clearly before now.

#### **4-ii. Estimates of voltage due to viscous-like interaction across the magnetopause**

We have demonstrated that the residual transpolar voltage after a period of southward IMF decays away with time elapsed since the IMF has been northward. After about 24 hours the voltage has decayed to  $\Phi_{PC} \approx 15 \text{ kV}$  and although in general  $\Phi_{PC}$  values are slightly sensitive to our choice of how many echoes are required ( $n_{min}$ ) to yield a valid  $\Phi_{PC}$  estimate, we have shown that this is not true for this estimate of the residual  $\Phi_{PC}$  after long ( $\sim 1$  day) intervals of northward IMF. There are some points that should be noted about this value. From the above discussion, if both  $\Phi_N$  or  $\Phi_D$  could be considered to be zero at these times then we get a maximum estimate of the viscously-like voltage  $\Phi_V < \Phi_{PC} \approx 15 \text{ kV}$ .

Viscously-driven flows, by definition, appear in the region of closed field lines on the flank of the magnetosphere called the low-latitude boundary layer (LLBL, see Figure 1). One problem is defining what are closed field lines and *Fuselier et al. (1999)* have pointed out that some of the particle flux signatures traditionally used to identify closed field lines are actually best explained as open field lines. *Mozzer (1984)* surveyed 24 LLBL crossings and found the voltage across the LLBL on one flank ranged between 0 and 16 kV, with an average of 3 kV. *Mozzer et al. (1994)* surveyed 41 such crossings and found an average value of 4 kV. If such a voltage existed on both flanks simultaneously this implies a viscous voltage  $\Phi_V$  in the range 0-32 kV with a mean value of 6-8 kV. These values are obtained by integrating the along-track electric field seen by magnetospheric spacecraft as they pass through the LLBL. *Hapgood and Lockwood (1993)* pointed out that an assumption in these measurements is that the LLBL is stationary and that the satellite moves through it so that the LLBL thickness is the speed of the satellite times the time it resides in the LLBL. However, in general a better approximation would be that the satellite be considered stationary and the boundary moves over it and that large estimates in LLBL thickness and  $\Phi_V$  can arise from a boundary that happens to be moving with the craft. They used plasma characteristics in the LLBL to show that for some cases of apparently large viscously-driven voltage the true value was, in fact, only about 3 kV on one flank: if the same applied on the other flank  $\Phi_V$  would be 6 kV. In theory, we should be able to use multi-spacecraft missions the pass through the LLBL to resolve boundary motions and compute LLBL thickness and voltage. Such missions include

AMPTE (Active Magnetospheric Particle Tracer Explorer), Cluster, MMS (Magnetospheric Multiscale Mission) and THEMIS (Time History of Events and Macroscale Interactions during Substorms). Although we can find several examples of the use of these spacecraft to determine LLBL thickness, a literature search has not revealed any further estimates of LLBL voltage. However, we note that *Lockwood and Hapgood* (1997) did use the AMPTE-IRM and AMPTE-UKS pair to show that the analysis of *Hapgood and Lockwood* (1993) was correct.

Detailed study of convection reversals in the ionosphere near dawn and dusk indicates that sometimes the plasma motion across them exceeds the motion of the boundary, implying they are not just moving adiabatic boundaries and there is a genuinely viscous-like process at work (*Lockwood et al.*, 1988; *Chen and Heelis*, 2018); however, in such cases the true boundary motion is very difficult to determine accurately and uncertainties are large making accurate determination of  $\Phi_V$  by integrating along the boundary almost impossible. *Newell et al.* (1991) and *Sundberg et al.* (2008) used LEO observations of electric fields and particle precipitations to infer the voltage across the low-altitude footprint of the LLBL and find values mainly below 10 kV with a few values over 20 kV. There are two problems with this which may explain the larger estimates of  $\Phi_V$ . Firstly, the identification of closed LLBL field lines from the particle precipitations is not definitive. Secondly, the ECPC model predicts that antisunward flow on closed field lines in the ionospheric projection of the LLBL can be generated by nightside reconnection and polar cap contraction because the convection reversal boundary can be shifted from the open-closed field line boundary by the conductivity distribution in the ionosphere.

From the above, a mean value of  $\Phi_V$  of around 8 kV is appropriate and so the estimate of  $\Phi_V \leq 15$  kV derived here from Figure 14, is somewhat higher than we would expect for an average value of past estimates. However, we stress here that this is a maximum value for  $\Phi_V$  because it is derived assuming  $\Phi_D = 0$  and  $\Phi_N = 0$  with lobe reconnection voltages lower than  $\Phi_V$ . There are reasons to believe none of these assumptions is valid. Firstly, it has been shown from outward fluxes of ionospheric ion species that opening of field lines continues between the magnetic cusps at a low level even when the IMF points northward (*Chandler et al.*, 1999; *Fuselier et al.*, 2000) and observations of simultaneous “double” cusps have been interpreted as subsolar reconnection continuing even though the IMF is northward and lobe reconnection is simultaneously taking place (*Lockwood and Moen*, 1999; *Pitout et al.*, 2002;

*Lockwood et al.*, 2003). Thus far we have only a limited number of such observations and so cannot say how common this situation is. Hence, although  $\Phi_D$  is small during northward IMF, it may be larger than zero some or all of the time. Secondly, as pointed out by *Lockwood* (2019), the tail lobes have never been seen to vanish, no matter how long the IMF remains northward. This means there is always a cross-tail current sheet with magnetic shear across it at which we would expect nightside reconnection to occur, even if the resulting  $\Phi_N$  is small. Thirdly *Wilder et al.* (2008) use SuperDARN data to show that the lobe reconnection voltages in the ionosphere saturates at about 15-20 kV and hence the voltages seen at large times since the IMF turned northward are likely to be caused by lobe reconnection than by viscous-like interaction.

Our definition of  $\Phi_{PC}$  means that a lobe reconnection  $\Phi_V$  would, if large enough either increase (the “hybrid” case) or set the value of  $\Phi_{PC}$  (the lobe-dominated case) such that its effect in the ionosphere exceeded  $\Phi_V$  (see section 1-i). Figure 7 shows that northward IMF  $\Phi_{PC}$  increases up to 15kV as the IMF approaches its largest positive values which is a behaviour expected of  $\Phi_L$  rather than  $\Phi_V$ . Hence the 15kV is consistent with being a “lobe dominated”  $\Phi_{PC}$  value set by lobe reconnection and not a “conventional” or “hybrid” viscous-like voltage to which  $\Phi_V$  could have contributed. As a consequence, we must treat 15 kV as an upper limit to the average value of  $\Phi_V$  and it is very likely to be considerably lower than this.

#### 4-iii. The effect of dynamic pressure

There are physical reasons to expect both the  $\Phi_D$  and  $\Phi_N$  to be increased by increased solar wind dynamic pressure  $p_{SW}$ . In both cases, the compression brought about by greater  $p_{SW}$  should increase the magnetic shear across the current sheet and so enhance the reconnection rate. One caveat to this idea is that the nightside reconnection must be taking place at a GSM X-coordinate at which the tail is still flaring (i.e., the radius increases with increasingly negative X) and so the dynamic pressure can squeeze the tail lobe and so increase the lobe field (*Caan et al.*, 1973) and the cross-tail current (*Lockwood*, 2013). At larger  $-X$  coordinates, further down the tail, the tail radius asymptotically reaches its maximum value and the component of the dynamic pressure perpendicular to the magnetopause falls to zero: in this case, the lobe field and magnetic shear across the cross-tail current sheet are set by the static pressure in the interplanetary medium.

824 Using the *am* geomagnetic index as a proxy indicator of magnetopause reconnection, *Scurry*  
825 *and Russell* (1991) inferred statistically that dayside reconnection voltage  $\Phi_D$  was indeed  
826 enhanced by increased  $p_{SW}$ . However much of the evidence for such an effect comes from  
827 transient responses to individual events in which  $p_{SW}$  increases suddenly (e.g., *Boudouridis et*  
828 *al.*, 2003). The problem with these events is there will be a number of transient responses, of  
829 which the effect of  $p_{SW}$  on  $\Phi_D$  is one and isolating just that one effect is difficult.

830 An important effect of  $p_{SW}$  on the tail was demonstrated directly by *Karlsson et al.* (2000)  
831 who showed that near-Earth tail energy content was reduced if  $p_{SW}$  decreased and that such  
832 sudden decreases caused quenching of any substorm expansion that had recently begun. This  
833 strongly suggests reduced  $p_{SW}$  can reduce the nightside voltage,  $\Phi_N$ . Conversely, increases in  
834  $p_{SW}$  have been seen to trigger onsets of full substorm expansion phases (*Schieldge and Siscoe*,  
835 1970; *Kokubun et al.*, 1977; *Yue et al.*, 2010) and have been identified as a cause of a rise in  
836  $\Phi_N$  (*Boudouridis et al.*, 2008b). In some cases, the rise in  $\Phi_N$  has been inferred from a loss of  
837 open flux as aurora expands into what appears to be open flux (*Hubert et al.*, 2006a).

838 Various observational studies suggest that increases in  $p_{SW}$  cause enhanced general  
839 magnetospheric convection and field-aligned current systems as well as enhanced  
840 geomagnetic activity (e.g., *Lukianova*, 2003; *Lee et al.*, 2004; *Hubert et al.*, 2006b;  
841 *Boudouridis et al.*, 2008a, *Stauning & Troshichev*, 2008). This phenomenon has been  
842 modelled using global MHD models of the magnetosphere as being caused by rises in both  
843  $\Phi_D$  and  $\Phi_N$  (*Palmroth et al.*, 2004; *Ober et al.*, 2006; *Connor et al.*, 2014; *Lockwood et al.*,  
844 2020b).

845 Figure 15 looks at the implications for any influence of  $p_{SW}$  on  $\Phi_D$  and  $\Phi_N$  of the correlations  
846 between  $p_{SW}$  and the auroral electrojet indices for both northward and southward IMF. It also  
847 compares the correlograms with those for  $p_{SW}$  and  $\Phi_{PC}$  for northward and southward IMF  
848 that were shown in Figure 6. The blue and orange and lines are for *AU* and *AL*, respectively,  
849 for southward IMF ( $B_Z < 0$ ). Both show a rapid response, although the correlation does not  
850 decay away for large positive lags as quickly for *AU* as it does for *AL*. Note that correlations  
851 are lower for the southward IMF data than for northward IMF (shown by the mauve and green  
852 lines) because the controlling influence of IMF  $B_Z$  is much greater for southward IMF. The  
853 mauve and green lines are for *AU* and *AL*, respectively and for northward IMF we see that  
854 *AL* responds to  $p_{SW}$  after a long lag, consistent with the squeezing of the tail by increased  $p_{SW}$

increasing  $\Phi_N$ . From the peak correlation this appears to be a relatively weak effect compared to the peaks for  $AU$ : however, it must be remembered that the lag for the dayside effect is short and much less variable than for any effect on the nightside and so we should expect a broad, but relatively low, peak for the effect on  $AL$ . Also note the peak for  $AU$  at short lags for northward IMF implies that the dayside reconnection is not only enhanced by increased  $p_{SW}$  when the IMF is southward, but that it may still present and enhanced by  $p_{SW}$  when it is IMF is northward. *Finch et al. (2008)* and *Lockwood et al. (2020a)* found that the effect of  $p_{SW}$  on mid-latitude range indices was via the nightside substorm current wedge. These authors also showed the effect was associated with  $\Phi_N$  and was the origin of the equinoctial time-of-day/time-of-year pattern in geomagnetic activity via the effect of the dipole tilt. The modelling analysis of *Lockwood et al. (2020b)* found both influence of  $p_{SW}$  via both  $\Phi_N$  and the energy stored in the tail lobe. The results presented here show an effect of  $p_{SW}$  on  $\Phi_{PC}$ , but that the effect is smaller than for  $am$ : this indicates that the effect of energy stored in the tail may be a larger factor for mid-latitude range indices such as  $am$ .

Since submitting the present paper, an article by *Boudouridis et al., (2021)* has been published, presenting an observation and modelling case study on enhancements in  $\Phi_D$  and  $\Phi_N$ , and hence  $\Phi_{PC}$ , induced by enhanced  $p_{SW}$ . As mentioned above, the studies of transient responses do not necessarily reveal the dependence of  $\Phi_D$  and  $\Phi_N$ , and hence  $\Phi_{PC}$ , on  $p_{SW}$  because of other transient responses although they do show a connection. We here have shown that there is a connection on a statistical basis. One potential problem is that  $p_{SW}$  has many parameters in common with the power input into the magnetosphere, but *Lockwood et al. (2020a; b, 2021)* have demonstrated that it has a separate and distinct influence on the  $am$  mid-latitude, range geomagnetic activity index. We here have demonstrated that  $p_{SW}$  has a similar influence on the nightside auroral  $AL$  index and the transpolar voltage  $\Phi_{PC}$ .

**Acknowledgements.** The authors acknowledge the use of data from the SuperDARN project. SuperDARN is a collection of radars funded by national scientific funding agencies of Australia, Canada, China, France, Italy, Japan, Norway, South Africa, United Kingdom and the United States of America. The work presented in this paper was supported by a number of grants. ML is supported by STFC consolidated grant number ST/M000885/1 and by the

885 SWIGS NERC Directed Highlight Topic Grant number NE/P016928/1/. Funding for KAM at  
 886 University of Saskatchewan was provided by the Canadian Foundation for Innovation (CFI),  
 887 the Province of Saskatchewan, and a Discovery Grant from the Natural Sciences and  
 888 Engineering Research Council (NSERC) of Canada. Initial work by KAM for this paper was  
 889 carried out at University of Reading on sabbatical leave from University of Saskatchewan.  
 890 We thank Evan Thomas, Kevin Sterne, Simon Shepherd, Keith Kotyk, Marina Schmidt,  
 891 Pasha Ponomarenko, Emma Bland, Maria-Theresia Walach, Ashton Reimer, Angeline  
 892 Burrell, and Daniel Billett for the SuperDARN radar processing toolkit used to analyse the  
 893 radar data. The authors are also grateful to the staff of: the Space Physics Data Facility,  
 894 NASA/Goddard Space Flight Center, who prepared and made available the OMNI2 dataset  
 895 used: these interplanetary data were downloaded from <http://omniweb.gsfc.nasa.gov/ow.html>;  
 896 the World Data Center for Geomagnetism, Kyoto who generate and make available the *AL*  
 897 index from <http://wdc.kugi.kyoto-u.ac.jp/aeasy/index.html> and the staff of L'École et  
 898 Observatoire des Sciences de la Terre (EOST), a joint of the University of Strasbourg and the  
 899 French National Center for Scientific Research (CNRS) and the International Service of  
 900 Geomagnetic Indices (ISGI) for making the am index data available from  
 901 [http://isgi.unistra.fr/data\\_download.php](http://isgi.unistra.fr/data_download.php)

## 902 **References**

- 903 Aikio, A., Pitkänen, T., Honkonen, I., Palmroth, M., Amm, O. (2013) IMF effect on the polar  
 904 cap contraction and expansion during a period of substorms, *Annales Geophysicae*, **31**: 1021-  
 905 1034 , doi: 10.5194/angeo-31-1021-2013
- 906 Baker, D. N., Klimas, A. J., Vassiliadis, D., Pulkkinen, T. I., and McPherron, R. L. (1997),  
 907 Re-examination of driven and unloading aspects of magnetospheric substorms, *J. Geophys.*  
 908 *Res.*, 102 (A4), 7169– 7177, doi: 10.1029/96JA02627.
- 909 Baker, D. N., Zwickl, R. D., Bame, S. J., Hones, E. W., Tsurutani, B. T., Smith, E. J., and  
 910 Akasofu, S.-I. (1983), An ISEE 3 high time resolution study of interplanetary parameter  
 911 correlations with magnetospheric activity, *J. Geophys. Res.*, **88** (A8), 6230– 6242,  
 912 doi:10.1029/JA088iA08p06230.
- 913 Birn, J., Hones, E. W., Craven, J. D., Frank, L. A., Elphinstone, R. D., and Stern, D. P.  
 914 (1991), On open and closed field line regions in Tsyganenko's field model and their possible  
 915 associations with horse collar auroras, *J. Geophys. Res.*, **96** (A3), 3811– 3817, doi:  
 916 10.1029/90JA02124.

917 Boudouridis, A., L.R. Lyons, E. Zesta, and J. M. Ruohoniemi (2007), Dayside reconnection  
918 enhancement resulting from a solar wind dynamic pressure increase, *J. Geophys. Res.*, **112**,  
919 A06201, doi:10.1029/2006JA012141.

920 Boudouridis, A., E. Zesta, L. R. Lyons, P. C. Anderson, and A. J. Ridley (2008a), Temporal  
921 evolution of the transpolar potential after a sharp enhancement in solar wind dynamic  
922 pressure, *Geophys. Res. Lett.*, **35**, L02101, doi:10.1029/2007GL031766.

923 Boudouridis, A., L. R. Lyons, E. Zesta, J. M. Ruohoniemi, and D. Lummerzheim (2008b),  
924 Nightside flow enhancement associated with solar wind dynamic pressure driven  
925 reconnection, *J. Geophys. Res.*, **113**, A12211, doi:10.1029/2008JA013489.

926 Boudouridis, A., Connor, H. K., Lummerzheim, D., Ridley, A. J., & Zesta, E. (2021).  
927 Changes in the Magnetic Field Topology and the Dayside/Nightside Reconnection Rates in  
928 Response to a Solar Wind Dynamic Pressure Front: A Case Study. *Journal of Geophysical*  
929 *Research: Space Physics*, **126**, e2020JA028768. doi: 10.1029/2020JA028768

930 Boyle, C. B., Reiff, P. H., and Hairston, M. R. (1997), Empirical polar cap potentials, *J.*  
931 *Geophys. Res.*, **102** (A1), 111– 125, doi: 10.1029/96JA01742.

932 Bristow, W. A., R. A. Greenwald, S. G. Shepherd, and J. M. Hughes (2004), On the observed  
933 variability of the cross-polar cap potential, *J. Geophys. Res.*, **109**, A02203, doi:  
934 10.1029/2003JA010206.

935 Browett, S.D., Fear, R. C., Grocott, A., and Milan, S. E. (2017), Timescales for the  
936 penetration of IMF By into the Earth's magnetotail, *J. Geophys. Res. Space Physics*, **122**,  
937 579– 593, doi: 10.1002/2016JA023198.

938 Caan M.N., McPherron R.L., Russell C.T. (1973), Solar wind and substorm-related changes  
939 in the lobes of the geomagnetic tail. *J. Geophys. Res.*, **78** (34): 8087–8096. doi:  
940 10.1029/ja078i034p08087.

941 Chandler, M.O., S.A. Fuselier, M. Lockwood and T.E. Moore (1999), Evidence of component  
942 magnetic merging equatorward of the cusp, *J. Geophys. Res.*, **104**, 22623–22648, doi:  
943 10.1029/1999JA900175.

944 Chen, Y.-J., & Heelis, R. A. (2018). Motions of the convection reversal boundary and local  
945 plasma in the high-latitude ionosphere, *Journal of Geophysical Research: Space Physics*, **123**,  
946 2953–2963. doi: 10.1002/2017JA024934

947 Chisham, G., Lester, M., Milan, S. E., Freeman, M. P., Bristow, W. A., Grocott, A.,  
948 McWilliams, K. A., Ruohoniemi, J. M., Yeoman, T. K., Dyson, P. L., Greenwald, R. A.,  
949 Kikuchi, T., Pinnock, M., Rash, J. P. S., Sato, N., Sofko, G.J., Villain, J.-P., Walker, A. D. M.  
950 (2007), A decade of the Super Dual Auroral Radar Network (SuperDARN): scientific  
951 achievements, new techniques and future directions, *Surveys in Geophys.*, **28** (1), 33–109, doi:  
952 10.1007/s10712-007-9017-8.

953 Connor, H. K., E. Zesta, D. M. Ober, and J. Raeder (2014), The relation between transpolar  
954 potential and reconnection rates during sudden enhancement of solar wind dynamic pressure:



955 OpenGGCM-CTIM results, *J. Geophys. Res. Space Physics*, **119**, 3411–3429, doi:  
956 10.1002/2013JA019728.

957 Consolini, G., and De Michelis, P. (2005), Local intermittency measure analysis of AE index:  
958 The directly driven and unloading component, *Geophys. Res. Lett.*, **32**, L05101,  
959 doi:10.1029/2004GL022063.

960 Cousins, E. D. P., Matsuo, T., and Richmond, A. D. (2013), SuperDARN assimilative  
961 mapping, *J. Geophys. Res. Space Physics*, **118**, 7954– 7962, doi:10.1002/2013JA019321.

962 Cowley, S. W. H. (1982), The causes of convection in the Earth's magnetosphere: A review of  
963 developments during the IMS, *Rev. Geophys.*, **20** (3), 531– 565,  
964 doi:10.1029/RG020i003p00531.

965 Cowley, S.W.H. (1984), Solar wind control of magnetospheric convection. *Achievements of*  
966 *the International Magnetospheric Study (IMS)*, Proceedings of an International Symposium,  
967 Graz, Austria, 26-28 June 1984, **ESA-SP-217**, Eds. B. Battrock and E.J. Rolfe., p.483,  
968 European Space Agency. ISSN 0379-6566  
969

970 Cowley, S. W. H., and Lockwood, M. (1992), Excitation and decay of solar-wind driven  
971 flows in the magnetosphere-ionosphere system, *Annales Geophys.*, **10**, 103-115.

972 Cowley, S.W.H., Freeman, M.P., Lockwood, M. and Smith, M.F. (1991a) The ionospheric  
973 signature of flux transfer events, in "*CLUSTER - dayside polar cusp*", ed. C.I. Barron, ESA  
974 SP-330, 105-112, European Space Agency Publications, Noordwijk, The Netherlands

975 Cowley, S.W.H., J.P. Morelli, and M. Lockwood (1991b) Dependence of convective flows  
976 and particle precipitation in the high-latitude dayside ionosphere on the X and Y components  
977 of the interplanetary magnetic field, *J. Geophys. Res.*, **96**, 5557-5564, doi:  
978 10.1029/90JA02063.

979 Davis, T. N., and Sugiura, M. (1966), Auroral electrojet activity index AE and its universal  
980 time variations, *J. Geophys. Res.*, **71** (3), 785–801, doi:10.1029/JZ071i003p00785.

981 DeJong, A. D., Ridley, A. J., and Clauer, C. R. (2008), Balanced reconnection intervals: four  
982 case studies, *Ann. Geophys.*, **26**, 3897–3912, doi: 10.5194/angeo-26-3897-2008, 2008.

983 Drayton, R. A., Koustov, A. V., Hairston, M. R., and Villain, J.-P. (2005), Comparison of  
984 DMSP cross-track ion-drifts and SuperDARN line-of-sight velocities, *Annales Geophysicae*,  
985 **23** (7), 2479–2486, doi: 10.5194/angeo-23-2479-2005.

986 Echer, E., Korth, A., Bolzan, M. J. A., & Friedel, R. H. W. (2017), Global geomagnetic  
987 responses to the IMF  $B_z$  fluctuations during the September/October 2003 high-speed stream  
988 intervals, *Annales Geophys.*, **35** (4), 853-868, doi: 10.5194/angeo-35-853-2017.

989 Etemadi, A., Cowley, S. W. H., Lockwood, M., Bromage, B. J. I., Willis, D. M. and Lühr, H.  
990 (1988), The dependence of high-latitude dayside ionospheric flows on the north-south  
991 component of the IMF: a high time resolution correlation analysis using EISCAT "POLAR"  
992 and AMPTE UKS and IRM data, *Planet. Space Sci.*, **36**, 471-498, doi: 10.1016/0032-  
993 0633(88)90107-9.

994 Farrugia, C.J., Gratton, F.T. & Torbert, R.B (2001), Viscous-type processes in the solar wind-  
995 magnetosphere interaction. *Space Science Reviews* 95, 443–456. doi:  
996 10.1023/A:1005288703357

997 Finch, I. D., Lockwood, M., and Rouillard, A. P. (2008), The effects of solar wind  
998 magnetosphere coupling recorded at different geomagnetic latitudes: separation of directly-  
999 driven and storage/release systems, *Geophys. Res. Lett.*, **35**, L21105,  
1000 doi:10.1029/2008GL035399.

1001 Fuselier, S.A., M. Lockwood, T.G. Onsager and W.K. Peterson (1999) The source population  
1002 for the cusp and cleft/LLBL for southward IMF, *Geophys. Res. Lett.*, **26**, 1665-1669, doi:  
1003 10.1029/1999GL900354.

1004 Fuselier, S.A., Trattner, K. J., and Petrinec, S. M. (2000), Cusp observations of high- and low-  
1005 latitude reconnection for northward interplanetary magnetic field, *J. Geophys. Res.*, **105** (A1),  
1006 253– 266, doi:10.1029/1999JA900422.

1007 Greenwald, R. A., Bristow, W. A., Sofko, G. J., Senior, C., Ceriser, J.-C., and Szabo, A.  
1008 (1995), Super Dual Auroral Radar Network radar imaging of dayside high-latitude convection  
1009 under northward interplanetary magnetic field: toward resolving the distorted two-cell versus  
1010 multicell controversy, *J. Geophys. Res.*, **100**, 19661–19674, doi: 10.1029/95ja01215.

1011 Gao, Y. (2012), Comparing the cross polar cap potentials measured by SuperDARN and  
1012 AMIE during saturation intervals, *J. Geophys. Res.*, **117**, A08325, doi:  
1013 10.1029/2012JA017690.

1014 Gordeev, E. I., Sergeev, V. A., Pulkkinen, T. I., and Palmroth, M. (2011), Contribution of  
1015 magnetotail reconnection to the cross-polar cap electric potential drop, *J. Geophys. Res.*, **116**,  
1016 A08219, doi:10.1029/2011JA016609.

1017 Haines, C. A., Owens, M. J., Barnard, L. A., Lockwood, M., and Ruffenach, A. (2019) The  
1018 variation of geomagnetic storm duration with intensity, *Solar Physics*, **294**, 154, pp1-15, doi:  
1019 10.1007/s11207-019-1546-z.

1020 Hairston, M. R., Heelis, R. A., and Rich, F. J. (1998), Analysis of the ionospheric cross polar  
1021 cap potential drop using DMSP data during the National Space Weather Program study  
1022 period, *J. Geophys. Res.*, **103** (A11), 26337– 26347, doi: 10.1029/97JA03241.

1023 Hanson, W. B., Coley, W. R., Heelis, R. A., Maynard, N. C., and Aggson, T. L. (1993), A  
1024 Comparison of in situ measurements of  $\vec{E}$  and  $-\vec{V} \times \vec{B}$  from Dynamics Explorer 2, *J. Geophys.*  
1025 *Res.*, **98** (A12), 21501– 21516, doi:10.1029/93JA01422.

1026 Hapgood, M.A., and M. Lockwood (1993) On the voltage and distance across the low-latitude  
1027 boundary layer, *Geophys. Res. Lett.*, **20**, 145-148, doi: 10.1029/93GL00063

1028 Hapgood, M. A., Bowe, G., Lockwood, M., Willis, D. M., and Tulunay, Y. (1991) Variability  
1029 of the interplanetary magnetic field at 1 A.U. over 24 years: 1963 – 1986, *Planet. Space Sci.*,  
1030 **39**, 411-423, doi: 10.1016/0032-0633(91)90003-S.

1031 Holzer, R. E., McPherron, R. L., and Hardy, D. A. (1986), A quantitative empirical model of  
 1032 the magnetospheric flux transfer process, *J. Geophys. Res.*, **91**(A3), 3287– 3293,  
 1033 doi:10.1029/JA091iA03p03287.

1034 Hones, E.W. Jr., J. D. Craven, L. A. Frank, D. S. Evans, P. T. Newell (1989) The horse-collar  
 1035 aurora: A frequent pattern of the aurora in quiet times, *Geophys. Res. Lett.*, **16** (1), 37-40, doi:  
 1036 10.1029/GL016i001p00037

1037 Huang, C.-S., A. D. DeJong, and X. Cai (2009), Magnetic flux in the magnetotail and polar  
 1038 cap during sawteeth, isolated substorms, and steady magnetospheric convection events, *J.*  
 1039 *Geophys. Res.*, **114**, A07202, doi: 10.1029/2009JA014232.

1040 Hubert, B., M. Palmroth, T. V. Laitinen, P. Janhunen, S. E. Milan, A. Grocott, S. W. H.  
 1041 Cowley, T. Pulkkinen, and J.-C. Gérard (2006a), Compression of the Earth's magnetotail by  
 1042 interplanetary shocks directly drives transient magnetic flux closure, *Geophys. Res. Lett.*, **33**,  
 1043 L10105, doi:10.1029/2006GL026008

1044 Hubert, B., Milan, S. E., Grocott, A., Block, C., Cowley, S. W. H., and Gérard, J.-C. (2006b),  
 1045 Dayside and nightside reconnection rates inferred from IMAGE FUV and Super Dual Auroral  
 1046 Radar Network data, *J. Geophys. Res.*, **111**, A03217, doi:10.1029/2005JA011140

1047 Imber, S. M., Milan, S. E., and Lester, M. (2013) Solar cycle variations in polar cap area  
 1048 measured by the superDARN radars, *Journal of Geophysical Research: Space Physics*, **118**  
 1049 (10), 6188 – 6196, doi: 10.1002/jgra.50509.

1050 Karlsson, S.B.P., Opgenoorth, H.J., Eglitis, P., Kauristie, K., Syrjäso, M., Pulkkinen, T.I.,  
 1051 Lockwood, M., Nakamura, R., Reeves, G., Romanov, S. (2000) Solar wind control of  
 1052 magnetospheric energy content: substorm quenching and multiple onsets. *J. Geophys. Res.*,  
 1053 **105**, 5335-5356, doi: 10.1029/1999JA900297

1054 King, J.H. and N.E. Papitashvili (2005) Solar wind spatial scales in and comparisons of  
 1055 hourly Wind and ACE plasma and magnetic field data, *J. Geophys. Res.*, **110**, A02104, doi:  
 1056 10.1029/2004JA010649

1057 Kokubun S. McPherron, R.L. Russell, C.T. (1977) Triggering of substorms by solar wind  
 1058 discontinuities. *J. Geophys. Res.*, **82** (1) 74-86, doi: 10.1029/ja082i001p00074.

1059 Klimas, A. J., Baker, D. N., Vassiliadis, D., and Roberts, D. A. (1994), Substorm recurrence  
 1060 during steady and variable solar wind driving: *Evidence* for a normal mode in the unloading  
 1061 dynamics of the magnetosphere, *J. Geophys. Res.*, **99**, 14855–14861. doi:  
 1062 10.1029/94JA01240.

1063 Koustov, A. V., Lavoie, D. B., Kouznetsov, A. F., Burchill, J. K., Knudsen, D. J., & Fiori, R.  
 1064 A. D. (2019a), A comparison of cross-track ion drift measured by the Swarm satellites and  
 1065 plasma convection velocity measured by SuperDARN, *Journal of Geophysical Research:*  
 1066 *Space Physics*, **124**, 4710–4724, doi: 10.1029/2018JA026245

1067 Koustov, A. V., Ullrich, S., Ponomarenko, P. V., Nishitani, N., Marcucci, F. M., Bristow, W.  
 1068 A. (2019b), Occurrence of F region echoes for the polar cap SuperDARN radars, *Earth*  
 1069 *Planets Space*, **71**, 112 (2019b). doi: 10.1186/s40623-019-1092-9

1070 Kubota, Y., Nagatsuma, T., Den, M., Tanaka, T., and Fujita, S. (2017), Polar cap potential  
1071 saturation during the Bastille Day storm event using global MHD simulation, *J. Geophys.*  
1072 *Res. Space Physics*, **122**, 4398–4409, doi:10.1002/2016JA023851.

1073 Laundal, K.M., Reistad, J.P., Hatch, S.M. et al. (2020) Time-scale dependence of solar wind-  
1074 based regression models of ionospheric electrodynamics. *Sci. Rep.* **10**, 16406. doi:  
1075 10.1038/s41598-020-73532-z

1076 Lee D.-Y., Lyons L.R., Yumoto K. (2004), Sawtooth oscillations directly driven by solar  
1077 wind dynamic pressure enhancements, *J. Geophys. Res.*, **109**, A04202. doi:  
1078 10.1029/2003JA010246.

1079 Lockwood, M. (1991), On flow reversal boundaries and cross-cap potential in average models  
1080 of high latitude convection, *Planet. Space Sci.*, **39**, 397-409, doi: 10.1016/0032-  
1081 0633(91)90002-R.

1082 Lockwood, M. (2013) Reconstruction and Prediction of Variations in the Open Solar  
1083 Magnetic Flux and Interplanetary Conditions, *Living Reviews in Solar Physics*, **10**, 4, 2013.  
1084 doi: 10.12942/lrsp-2013-4

1085 Lockwood, M. (2019), Does adding solar wind Poynting flux improve the optimum solar  
1086 wind-magnetosphere coupling function? *J. Geophys. Res. (Space Physics)*, **124** (7), 5498-  
1087 5515, doi: 10.1029/2019JA026639.

1088 Lockwood, M., and Cowley, S.W.H. (1992) Ionospheric Convection and the substorm cycle  
1089 in “Substorms 1, Proceedings of the First International Conference on Substorms, ICS-1”, ed  
1090 C. Mattock, ESA-SP-335, 99-109, European Space Agency Publications, Noordwijk, The  
1091 Netherlands.

1092 Lockwood M. and M.A. Hapgood (1997) How the Magnetopause Transition Parameter  
1093 Works, *Geophys. Res. Lett.*, **24**, 373-376, doi: 10.1029/97GL00120

1094 Lockwood, M., and Moen, J. (1999) Reconfiguration and closure of lobe flux by reconnection  
1095 during northward IMF: evidence for signatures in cusp/cleft auroral emissions, *Annales*  
1096 *Geophys.*, **17**, 996-1011, doi: 10.1007/s00585-999-0996-2.

1097 Lockwood, M., and Morley, S. E. (2004), A numerical model of the ionospheric signatures of  
1098 time-varying magnetic reconnection: I. Ionospheric convection, *Annales Geophys.*, **22**, 73-91,  
1099 doi: 10.5194/angeo-22-73-2004.

1100 Lockwood, M., van Eyken, A. P., Bromage, B. J. I., Willis, D. M., and Cowley, S. W. H.  
1101 (1986), Eastward propagation of a plasma convection enhancement following a southward  
1102 turning of the interplanetary magnetic field, *Geophys. Res. Lett.*, **13**, 72-75, doi:  
1103 10.1029/GL013i001p00072.

1104 Lockwood, M., S.W.H. Cowley, H. Todd, D.M. Willis and C.R. Clauer (1988) Ion flows and  
1105 heating at a contracting polar cap boundary, *Planet. Space Sci.*, **36**, 1229-1253, doi:  
1106 10.1016/0032-0633(88)90076-1

1107 Lockwood, M., Cowley, S. W. H., and Freeman, M. P. (1990), The excitation of plasma  
 1108 convection in the high latitude ionosphere, *J. Geophys Res.*, **95**, 7961-7971, doi:  
 1109 10.1029/JA095iA06p07961, 1990

1110 Lockwood, M., Denig, W.F., Farmer, A.D., Davda, V.N., Cowley, S.W.H and Lühr, H.  
 1111 (1993) Ionospheric signatures of pulsed magnetic reconnection at the Earth's magnetopause,  
 1112 *Nature*, **361** (6411), 424-428. doi: 10.1038/361424a0

1113 Lockwood, M., B.S. Lanchester, H. Frey, K. Throp, S. Morley, S.E. Milan, and M.E. Lester  
 1114 (2003) IMF Control of Cusp Proton Emission Intensity and Dayside Convection: implications  
 1115 for component and anti-parallel reconnection, *Annales Geophys.*, **21**, 955-982, doi:  
 1116 10.5194/angeo-21-955-2003

1117 Lockwood, M., Throp, K. Lanchester, B. S., Morley, S. K., Milan, S. E., Lester, M., and H. U.  
 1118 Frey, H. U. (2006), Modelling the observed proton aurora and ionospheric convection  
 1119 responses to changes in the IMF field clock angle: 2. The persistence of ionospheric  
 1120 convection, *J. Geophys. Res.*, **111**, A02306, doi:10.1029/2003JA010307.

1121 Lockwood, M., Hairston, M. R., Finch, I. D., and Rouillard, A. P. (2009), Transpolar voltage  
 1122 and polar cap flux during the substorm cycle and steady convection events, *J. Geophys. Res.*,  
 1123 **114**, A01210, doi: 10.1029/2008JA013697.

1124 Lockwood, M., Owens, M. J., Barnard, L. A., Bentley, S., Scott, C. J., and Watt, C. E. (2016),  
 1125 On the Origins and Timescales of Geoeffective IMF, *Space Weather*, **14**, 406-432, doi:  
 1126 10.1002/2016SW001375.

1127 Lockwood, M., Owens, M. J., Barnard, L. A., Scott, C. J., and Watt, C. E. (2017), Space  
 1128 Climate and Space Weather over the past 400 years: 1. The Power input to the  
 1129 Magnetosphere, *J. Space Weather Space Clim.*, **7**, A25, doi: 10.1051/swsc/2017019.

1130 Lockwood, M., Chambodut, A., Barnard, L. A., Owens, M. J., Clarke, E., and Mendel, V.  
 1131 (2018a), A homogeneous aa index: 1. Secular variation, *J. Space Weather Space Clim.*, **8**,  
 1132 A53, doi: 10.1051/swsc/2018038.

1133 Lockwood, M., Finch, I. D., Chambodut, A., Barnard, L. A., Owens, M. J., and Clarke, E.  
 1134 (2018b), A homogeneous aa index: 2. hemispheric asymmetries and the equinoctial variation,  
 1135 *J. Space Weather Space Clim.*, **8**, A58, doi: 10.1051/swsc/2018044.

1136 Lockwood, M., Bentley, S., Owens, M. J., Barnard, L. A., Scott, C. J., Watt, C. E. and  
 1137 Allanson, O. (2019a), The development of a space climatology: 1. Solar-wind magnetosphere  
 1138 coupling as a function of timescale and the effect of data gaps, *Space Weather*, **17**, 133-156,  
 1139 doi: 10.1029/2018SW001856.

1140 Lockwood, M., S. Bentley, M.J. Owens, L.A. Barnard, C.J. Scott, C.E. Watt, O. Allanson and  
 1141 M.P. Freeman (2019b) The development of a space climatology: 2. The distribution of power  
 1142 input into the magnetosphere on a 3-hourly timescale, *Space Weather*, **17**, 157-179. doi:  
 1143 10.1029/2018SW002016

1144 Lockwood, M., S. Bentley, M.J. Owens, L.A. Barnard, C.J. Scott, C.E. Watt, O. Allanson and  
 1145 M.P. Freeman (2019c) The development of a space climatology: 3. The evolution of

distributions of space weather parameters with timescale, *Space Weather*, **17**, 180-209. doi: 10.1029/2018SW002017

Lockwood, M., K.A. McWilliams, M.J. Owens, L.A. Barnard, C.E. Watt, C.J. Scott, A. McNeill and J.C. Coxon (2020a) Semi-annual, annual and Universal Time variations in the magnetosphere and in geomagnetic activity: 2. Response to solar wind power input and relationships with solar wind dynamic pressure and magnetospheric flux transport, *J. Space Weather Space Clim.*, **10**, 30, doi: 10.1051/swsc/2020033

Lockwood, M., M.J. Owens, L.A. Barnard, C.E. Watt, C.J. Scott, J.C. Coxon and K.A. McWilliams (2020b) Semi-annual, annual and Universal Time variations in the magnetosphere and in geomagnetic activity: 3. Modelling, *J. Space Weather and Space Climate*, **10**, 61 doi: 10.1051/swsc/2020062

Lockwood, M., C.A. Haines, L.A. Barnard, J. Owens, C.J. Scott, A. Chambodut, and K.A. McWilliams (2021) Semi-annual, annual and Universal Time variations in the magnetosphere and in geomagnetic activity: 4. Polar Cap motions and origins of the Universal Time effect, *J. Space Weather and Space Climate*, **11**, 15, doi: 10.1051/swsc/2020077

Lopez, R. E., Wiltberger, M., Lyon, J. G., Goodrich, C. C., Papadopoulos, K. (1999) MHD simulations of the response of high-latitude potential patterns and polar cap boundaries to sudden southward turnings of the interplanetary magnetic field, *Geophys. Res. Lett.*, **26** (7), 967 – 970, doi: 10.1029/1999GL900113.

Lopez, R. E., Lyon, J. G., Wiltberger, M. J., Goodrich, C. C. (2001) Comparison of global MHD simulation results with actual storm and substorm events, *Adv. Space Res.*, **28**, (12), 1701-1706, doi: 10.1016/S0273-1177(01)00535-X

Lühr, H., M. Lockwood, P.A. Sandholt, T.L. Hansen and T. Moretto (1996) Multi-instrument ground-based observations of a Travelling Convection Vortex event, *Annales Geophys.*, **14**, 162-181, doi: 10.1007/s00585-996-0162-z.

Liu, E., H. Hu, J. Liu, X. Teng, L. Qiao (2019) Predicting SuperDARN cross polar cap potential by applying regression analysis and machine learning, *J. Atmos. Sol.-Terr. Phys.*, **193**, 105057, doi: 10.1016/j.jastp.2019.105057.

Lukianova R. (2003), Magnetospheric response to sudden changes in solar wind dynamic pressure inferred from polar cap index, *J. Geophys. Res.*, **108**(A12), 1428 doi: 10.1029/2002JA009790.

Mayaud, P.-N. (1980), Derivation, Meaning and Use of Geomagnetic Indices, *Geophysical Monograph*, 22, American Geophysical Union, Washington, DC. doi: 10.1029/GM022.

McPherron, R. L. (2020), Early studies in solar wind coupling and substorms, *Journal of Geophysical Research: Space Physics*, 125, e2019JA027615, doi: 10.1029/2019JA027615.

McPherron, R.L., Baker, D. N., Bargatze, L. F., Clauer, C. R., and Holzer, R. E. (1998), IMF control of geomagnetic activity, *Adv. Space Res.*, **8** (9–10), 71-86, doi: 10.1016/0273-1177(88)90114-7.

1184 McWilliams, K.A., Yeoman, T. K., and Cowley, S. W. H (2000) Two-dimensional electric  
 1185 field measurements in the ionospheric footprint of a flux transfer event, *Annales Geophys.*, **18**  
 1186 (12), 1584 -1598. doi: 10.1007/s00585-001-1584-2

1187 McWilliams, K. A., Pfeifer, J. B., and McPherron, R. L. (2008), Steady magnetospheric  
 1188 convection selection criteria: Implications of global SuperDARN convection measurements,  
 1189 *Geophys. Res. Lett.*, **35**, L09102, doi:10.1029/2008GL033671.

1190 Milan, S. E. (2004), Dayside and nightside contributions to the cross polar cap potential:  
 1191 placing an upper limit on a viscous-like interaction, *Ann. Geophys.*, **22**, 3771–3777, doi:  
 1192 10.5194/angeo-22-3771-2004.

1193 Milan, S. E., Lester, M., Cowley, S. W. H. Oksavik, K., Brittnacher, M., Greenwald, R. A.,  
 1194 Sofko, G., and Villain, J.-P. (2003), Variations in the polar cap area during two substorm  
 1195 cycles, *Annales Geophys.*, **21** (5), 1121-1140, doi: 10.5194/angeo-21-1121-2003.

1196 Milan, S. E., Hutchinson, J., Boakes, P. D., and Hubert, B. (2009), Influences on the radius of  
 1197 the auroral oval, *Annales Geophys.*, **21** (5), 1121-1140. doi: 10.5194/angeo-21-1121-2003.

1198 Milan, S. E., Gosling, J. S., and Hubert, B. (2012), Relationship between interplanetary  
 1199 parameters and the magnetopause reconnection rate quantified from observations of the  
 1200 expanding polar cap, *J. Geophys. Res.*, **117**, A03226, doi: 10.1029/2011JA017082.

1201 Milan, S. E., Carter, J. A., Bower, G. E., Imber, S. M., Paxton, L. J., Anderson, B. J., et al.  
 1202 (2020). Dual-lobe reconnection and horse-collar auroras. *Journal of Geophysical Research:*  
 1203 *Space Physics*, **125**, e2020JA028567. doi: 10.1029/2020JA028567

1204 Milan, S. E., Carter, J. A., Sangha, H., Bower, G. E., & Anderson, B. J. (2021).  
 1205 Magnetospheric flux throughput in the Dungey cycle: Identification of convection state during  
 1206 2010. *Journal of Geophysical Research: Space Physics*, **126**, e2020JA028437. doi:  
 1207 10.1029/2020JA028437

1208 Mishin V. V. Karavaev Yu. A. (2017) Saturation of the magnetosphere during superstorms:  
 1209 new results from the magnetogram inversion technique, *Solar-Terrestrial Physics*, **3** (3), 28-  
 1210 36, doi: 10.12737/stp-33201704

1211 Morley, S. E., and Lockwood, M. (2005), A numerical model of the ionospheric signatures of  
 1212 time-varying magnetic reconnection: II. Measuring expansions in the ionospheric flow  
 1213 response, *Annales Geophys.*, **23**, 2501-2510, doi: 10.5194/angeo-23-2501-2005

1214 Mozer, F.S. (1984), Electric field evidence on the viscous interaction at the magnetopause.  
 1215 *Geophys. Res. Lett.*, **11**, 135-138. doi: 10.1029/GL011i002p00135

1216 Mozer, F.S., H. Hayakawa, S. Kokubun, M. Nakamura, T. Okada, T. Yamamoto and K.  
 1217 Tsuruda (1994) The morningside low-latitude boundary layer as determined from electric and  
 1218 magnetic field measurements on Geotail, *Geophys. Res. Lett.*, **21** (25), 2983-2986, doi:  
 1219 10.1029/94GL01296

1220 Newell, P. T., W. J. Burke, E. R. Sanchez, et al. (1991), The low-latitude boundary layer and  
 1221 the boundary plasma sheet at low altitude: Prenoon precipitation regions and convection  
 1222 reversal boundaries, *J. Geophys. Res.*, **96**, 21,013–21,023, doi: 10.1029/91ja01818  
 1223 Nishida, A. (1968a), Coherence of geomagnetic DP 2 fluctuations with interplanetary  
 1224 magnetic variations, *J. Geophys. Res.*, **73** (17), 5549– 5559, doi: 10.1029/JA073i017p05549.  
 1225 Nishida, A. (1968b), Geomagnetic DP 2 fluctuations and associated magnetospheric  
 1226 phenomena, *J. Geophys. Res.*, **73** (5), 1795– 1803, doi: 10.1029/JA073i005p01795.  
 1227 Ober, D. M., G. R. Wilson, N. C. Maynard, W. J. Burke, and K. D. Siebert (2006), MHD  
 1228 simulation of the transpolar potential after a solar-wind density pulse, *Geophys. Res. Lett.*,  
 1229 **539**(33), L04106, doi:10.1029/2005GL024655.  
 1230 Palmroth, M., Pulkkinen, T.I., Janhunen, P., McComas, D.J., Smith, C.W., Koskinen, H.E.J.  
 1231 (2004), Role of solar wind dynamic pressure in driving ionospheric Joule heating, *J. Geophys.*  
 1232 *Res.*, **109**, A11302, doi: 10.1029/2004JA010529.  
 1233 Pitout, F., Newell, P.T. and Buchert, S.C. (2002) Simultaneous high-and low-latitude  
 1234 reconnection: ESR and DMSP observations, *Annales Geophys.*, **20** (9), 1311-1320, doi:  
 1235 10.5194/angeo-20-1311-2002  
 1236 Provan, G., Yeoman, T. K., Milan, S. E., Ruohoniemi, J. M., and Barnes, R. (2002) An  
 1237 assessment of the “map-potential” and “beam-swinging” techniques for measuring the  
 1238 ionospheric convection pattern using data from the SuperDARN radars, *Annales Geophys.*, **20**,  
 1239 191–202, doi: 10.5194/angeo-20-191-2002.  
 1240 Reiff, P. H., Spiro, R. W., and Hill, T. W. (1981), Dependence of polar cap potential drop on  
 1241 interplanetary parameters, *J. Geophys. Res.*, **86** (A9), 7639– 7648, doi:  
 1242 10.1029/JA086iA09p07639.  
 1243 Ruohoniemi, J. M., and Baker K. B, (1998) Large-scale imaging of high-latitude convection  
 1244 with Super Dual Auroral Radar Network HF radar observations, *J. Geophys. Res.*, **103**,  
 1245 20797–20811, doi: 10.1029/98ja01288.  
 1246 Saunders, M. A., Freeman, M. P., Southwood, D. J., Cowley, S. W. H., Lockwood, M.,  
 1247 Samson, J. C., Farrugia, C. J., and Hughes, T. J. (1992) Dayside ionospheric convection  
 1248 changes in response to long period IMF oscillations: determination of the ionospheric phase  
 1249 velocity, *J. Geophys. Res.*, **97**, 19373-19380, doi: 10.1029/92JA01383.  
 1250 Schieldge, J.P., Siscoe, G.L. (1970) A correlation of the occurrence of simultaneous sudden  
 1251 magnetospheric compressions and geomagnetic bay onsets with selected geophysical indices.  
 1252 *J. Atmos. Terr. Phys.*, **32** (11), 1819-1830, doi: 10.1016/0021-9169(70)90139-x.  
 1253 Scurry, L., and Russell, C. T. (1991), Proxy studies of energy transfer to the magnetosphere,  
 1254 *J. Geophys. Res.*, **96** (A6), 9541– 9548, doi:10.1029/91JA00569.  
 1255 Shepherd, S. G., and Ruohoniemi, J. M. (2000), Electrostatic potential patterns in the high-  
 1256 latitude ionosphere constrained by SuperDARN measurements, *J. Geophys. Res.*, **105**, 23005–  
 1257 23014, doi: 10.1029/2000ja000171.



1258 Siscoe, G. L., and Huang, T. S. (1985), Polar cap inflation and deflation, *J. Geophys. Res.*, **90**  
1259 (A1), 543– 547, doi:10.1029/JA090iA01p00543.

1260 Stauning P., Troshichev, O.A. (2008), Polar cap convection and PC index during sudden  
1261 changes in solar wind dynamic pressure, *J. Geophys. Res.*, **113**, A08227, doi:  
1262 10.1029/2007JA012783.

1263 Sundberg, K. Å. T., Blomberg, L. G., and Cumnock, J. A. (2008), Statistical analysis of the  
1264 sources of the cross-polar potential for southward IMF, based on particle precipitation  
1265 characteristics, *Geophys. Res. Lett.*, **35**, L08103, doi:10.1029/2008GL033383

1266 Throp, K., M. Lockwood, B. S. Lanchester, S. K. Morley, and H. U. Frey (2005) Modeling  
1267 the observed proton aurora and ionospheric convection responses to changes in the IMF clock  
1268 angle: 1. Persistence of cusp proton aurora, *J. Geophys. Res.*, **110**, A12311, doi:  
1269 10.1029/2003JA010306

1270 Todd, H., Cowley, S. W. H., Etemadi, A., Bromage, B. J. I., Lockwood, M., Willis, D. M.,  
1271 and Lühr, H. (1988) Flow in the high-latitude ionosphere: measurements at 15-second  
1272 resolution made using the EISCAT "POLAR" experiment, *J. atmos. terr. Phys.*, **50**, 423-446,  
1273 doi: 10.1016/0021-9169(88)90026-8.

1274 Weigel, R. S. (2007), Solar wind time history contribution to the day-of-year variation in  
1275 geomagnetic activity, *J. Geophys. Res.*, **112**, A10207, doi: 10.1029/2007JA012324.

1276 Weimer, D. R., Maynard, N. C., Burke, W. J., & Liebrecht, C. (1990), Polar cap potentials  
1277 and the auroral electrojet indices, *Planetary and space science*, **38**(9), 1207-1222. doi:  
1278 10.1016/0032-0633(90)90028-o

1279 Wilder, F. D., Clauer, C. R., and Baker, J. B. H. (2008), Reverse convection potential  
1280 saturation during northward IMF, *Geophys. Res. Lett.*, **35**, L12103,  
1281 doi:10.1029/2008GL034040.

1282 Wilder, F. D., Clauer, C. R., Baker, J. B. H., Cousins, E. P., and Hairston, M. R. (2011) The  
1283 nonlinear response of the polar cap potential under southward IMF: A statistical view, *J.*  
1284 *Geophys. Res.*, **116**, A12229, doi:10.1029/2011JA016924.

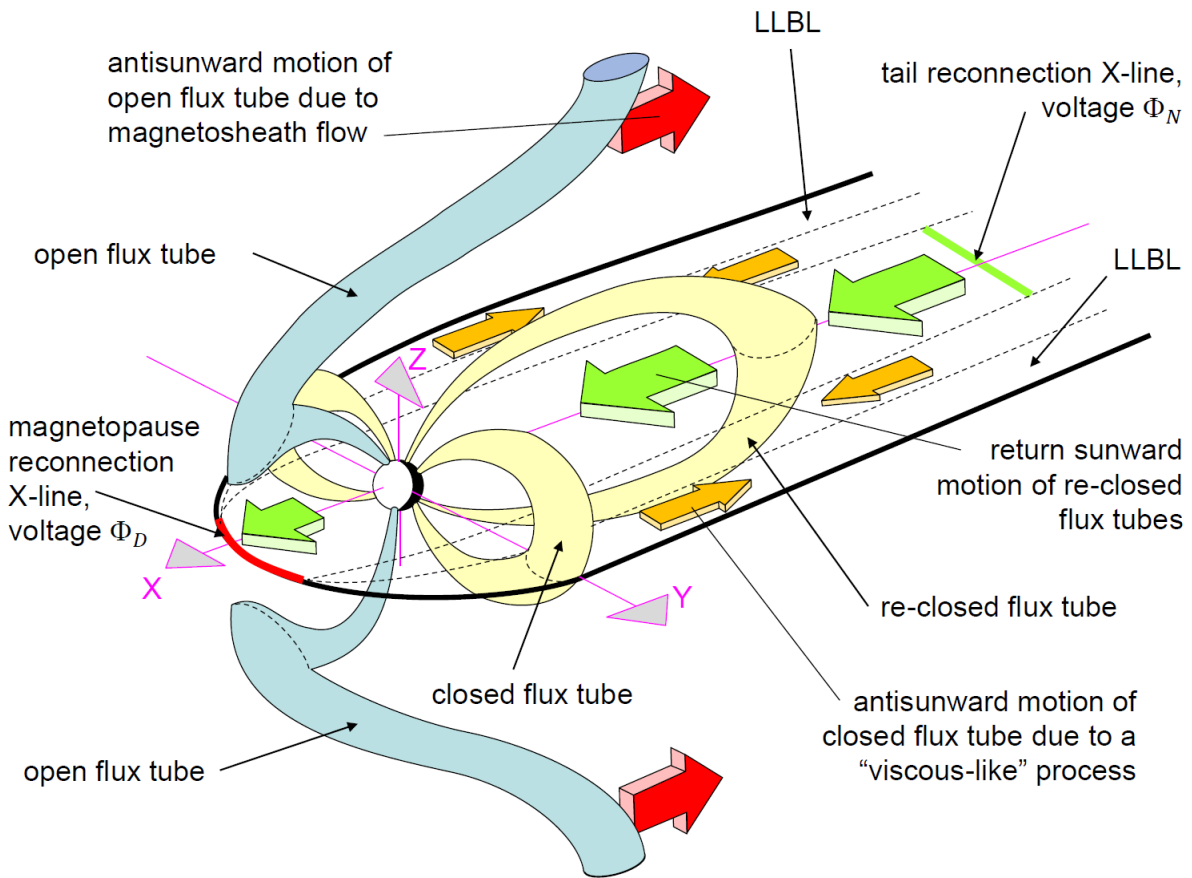
1285 Wygant, J. R., Torbert, R. B., and Mozer, F. S. (1983), Comparison of S3-3 polar cap  
1286 potential drops with the interplanetary magnetic field and models of magnetopause  
1287 reconnection, *J. Geophys. Res.*, **88** (A7), 5727– 5735, doi:10.1029/JA088iA07p05727.

1288 Xu, L., Koustov, A. V. Xu, J. S., Drayton, R. A., and Huo, L. (2007a), A 2-D comparison of  
1289 ionospheric convection derived from SuperDARN and DMSP measurements, *Adv. Space*  
1290 *Res.*, **42** (7), 1259-1266, doi: 10.1016/j.asr.2007.06.044.

1291 Xu, L., Xu, J., Alexandre, K., Papitashvili, V., and Rich, F. (2007b) A comparison of  
1292 SuperDARN-derived plasma convection and DMSP ion drift measurements, *Wuhan Univ. J.*  
1293 *of Nat. Sci.*, **12**, 279–283. doi: 10.1007/s11859-006-0024-2

1294 Yue, C., Zong, Q.G., Zhang, H., Wang, Y.F., Yuan, C.J., Pu, Z.Y., Fu, S.Y., Lui, A.T.Y.,  
1295 Yang, B., Wang, C.R. (2010), Geomagnetic activity triggered by interplanetary shocks. *J.*  
1296 *Geophys. Res.* **115**, A00I05. doi: 10.1029/2010JA015356.

1297



1298

1299 **Figure 1.** Schematic of three convection drivers in the magnetosphere and ionosphere,  
 1300 adapted from Cowley (1982) with the addition of a reconnection X-line in the cross-tail  
 1301 current sheet (in green, the voltage across which is  $\Phi_N$ ). This X-line re-closes open field  
 1302 lines and is included here because in the ECPC model (Cowley and Lockwood, 1992) it  
 1303 contributes to the ionospheric transpolar voltage  $\Phi_{PC}$  at any one time by adding to the effect  
 1304 of the reconnection voltage  $\Phi_D$  along the dayside magnetopause X-line (in red) which  
 1305 generates open field lines. The third source of  $\Phi_{PC}$  is “viscous-like” momentum transfer  
 1306 across the magnetopause onto closed field lines that generates a total antisunward magnetic  
 1307 flux transfer of closed flux of voltage  $\Phi_V$  in the low latitude boundary layers (LLBL).

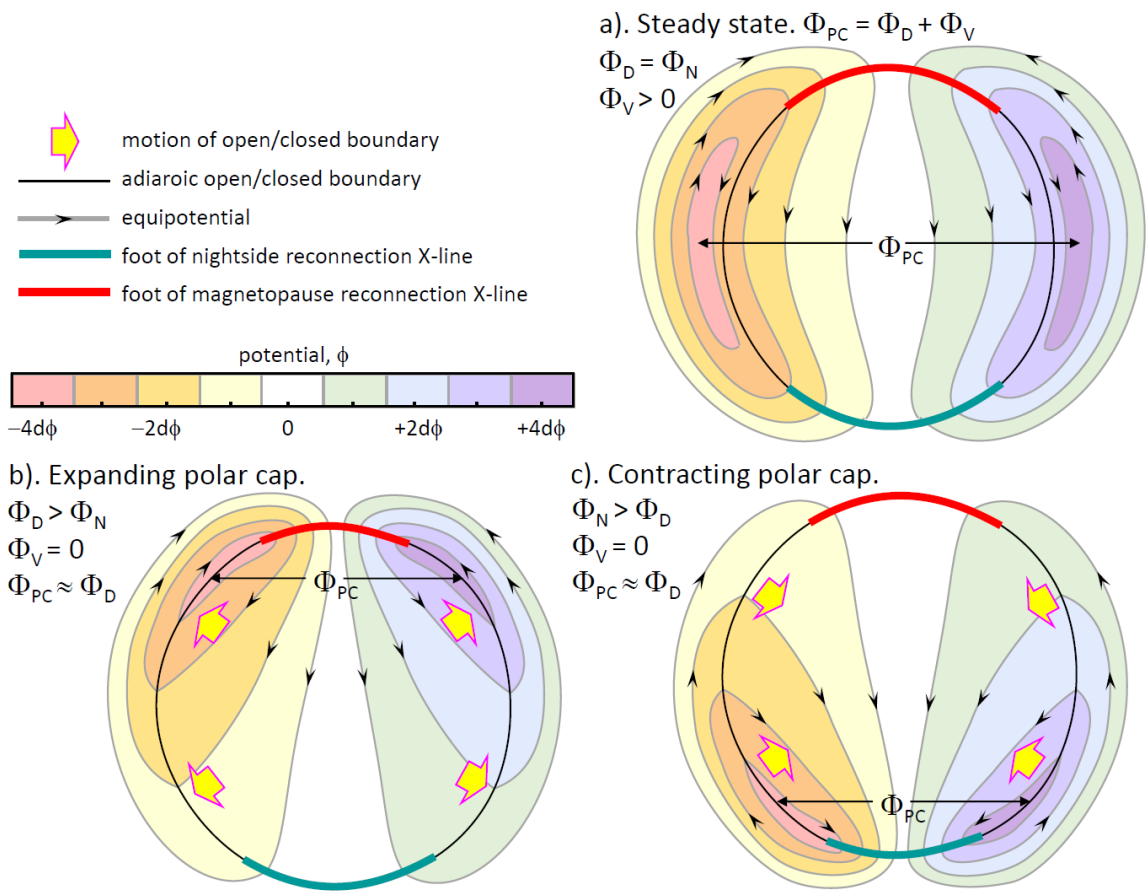
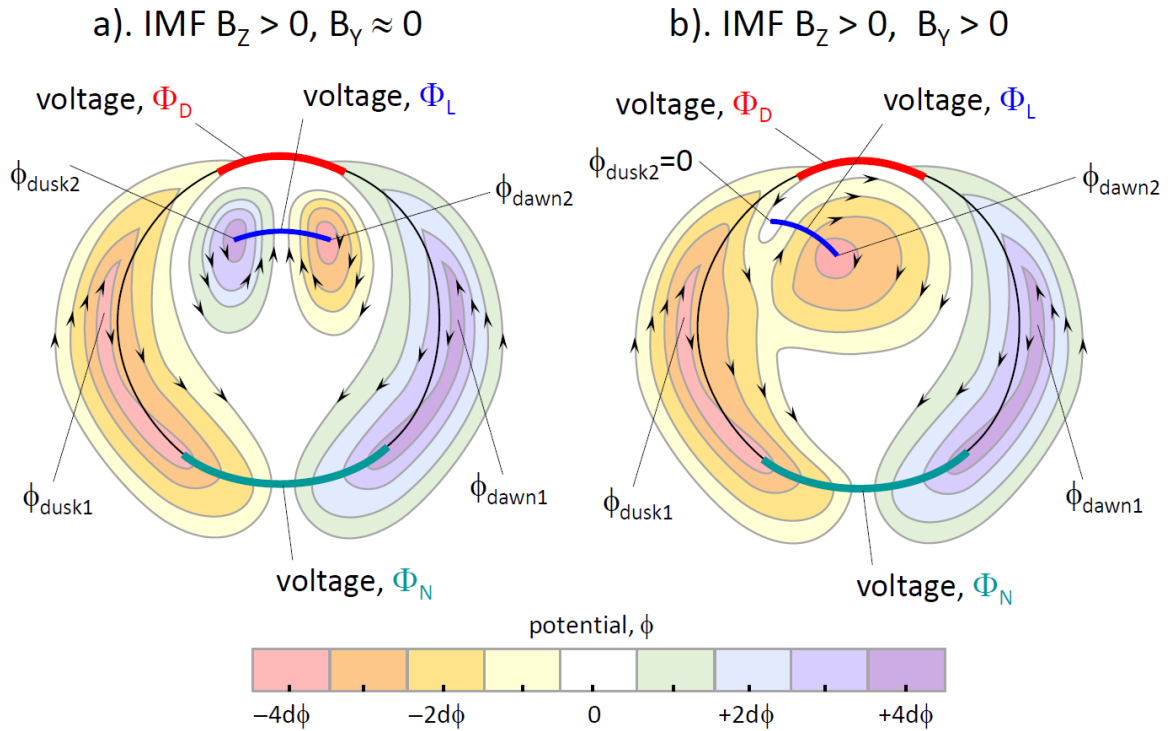


**Figure 2.** Schematic illustration of northern hemisphere ionospheric flow streamlines (equipotentials,  $d\phi$  apart) under the influence of three driving voltages  $\Phi_D$ ,  $\Phi_N$  and  $\Phi_V$  discussed in Figure 1, as predicted by the ECPC model of ionospheric flow excitation for the special case where polar cap remains circular: (a) is for steady state (also known as balanced reconnection), (b) for an expanding polar cap and (c) for a contracting polar cap.



1315

1316 **Figure 3.** Schematic illustrations of northern-hemisphere ionospheric flow streamlines  
 1317 (equipotentials  $d\phi$  apart) during northward IMF ( $B_z > 0$ ) and under the influence of the three  
 1318 driving voltages  $\Phi_D$ ,  $\Phi_N$  and  $\Phi_V$  discussed in Figure 1, plus a lobe reconnection voltage  $\Phi_L$ .  
 1319 Both cases are for a contracting polar cap with  $\Phi_N > \Phi_D$  giving poleward motion of the  
 1320 adiaroic polar cap boundaries. In part (a), lobe reconnection with IMF  $B_y \approx 0$  gives two  
 1321 symmetric lobe circulation cells in the polar cap. Part (b) is an example of a case with large  
 1322 IMF  $|B_y|$ , showing the effect of  $B_y > 0$  in the northern hemisphere, which yields a dominant  
 1323 dawn lobe cell, the sunward flow portion of which can merge with main dusk cell at the lower  
 1324 potentials because of the poleward contraction of the dusk adiaroic polar cap boundary. In  
 1325 part (a)  $\Phi_L$  is close to the value of  $\Phi_{PC}$  that is set by  $\Phi_D$ ,  $\Phi_N$  and  $\Phi_V$ : in terms of the potential  
 1326 separation  $d\phi$ , the schematic in part (a) is for  $\Phi_N = 8d\phi$ ,  $\Phi_D = 2d\phi$ ,  $\Phi_L = 8d\phi$  and  
 1327  $\Phi_V = 2d\phi$ . In part (b)  $\Phi_N = 8d\phi$ ,  $\Phi_D = 2d\phi$ ,  $\Phi_L = 4d\phi$  and  $\Phi_V = 2d\phi$ .

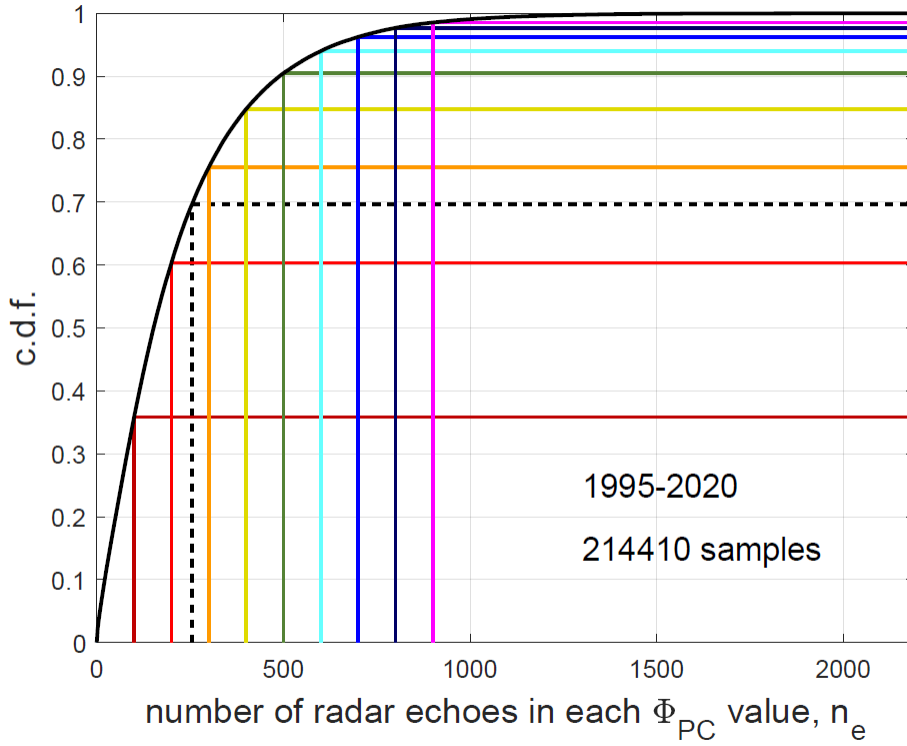
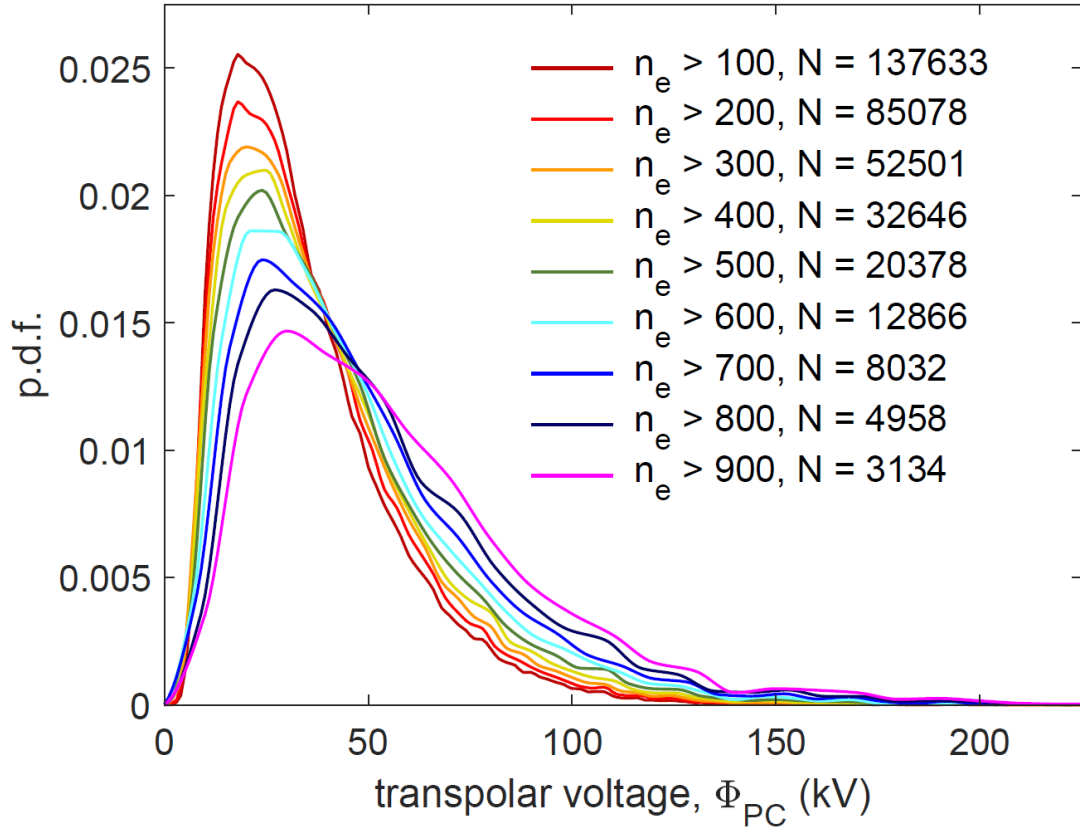


**Figure 4.** Cumulative probability distribution of the number of radar echoes,  $n_e$ , used in compiling the convection patterns, and hence the transpolar voltage  $\Phi_{PC}$  estimates in the dataset employed here of 214410  $\Phi_{PC}$  values obtained from the SuperDARN radar array using the map-potential technique between 1995 and 2020. The vertical lines are various threshold values  $n_{min}$  used in this paper which  $n_e$  must exceed for the  $\Phi_{PC}$  value obtained to be considered valid. The vertical-coloured lines are at  $n_{min}$  of [100:100:900] and the black dashed line is at 255. The condition  $n_e > n_{min} = 255$  was found to be optimum in a comparison with 2-years data from satellite passes (for 2001 and 2002, see Appendix A) and which yields  $N = 60653$  valid  $\Phi_{PC}$  estimates which is close to 30% of all observations. The coloured thresholds are here used in a sensitivity study to understand the effect of the adopted  $n_{min}$  threshold.



1340

1341 **Figure 5.** Probability density functions giving the normalised distributions of the  $\Phi_{PC}$  values  
 1342 for threshold values for the number of echoes  $n_e$  required of  $n_{\min} = [100:100:900]$ . The  
 1343 resulting total number of  $\Phi_{PC}$  values in the data set meeting that requirement,  $N$ , is given in  
 1344 each case.

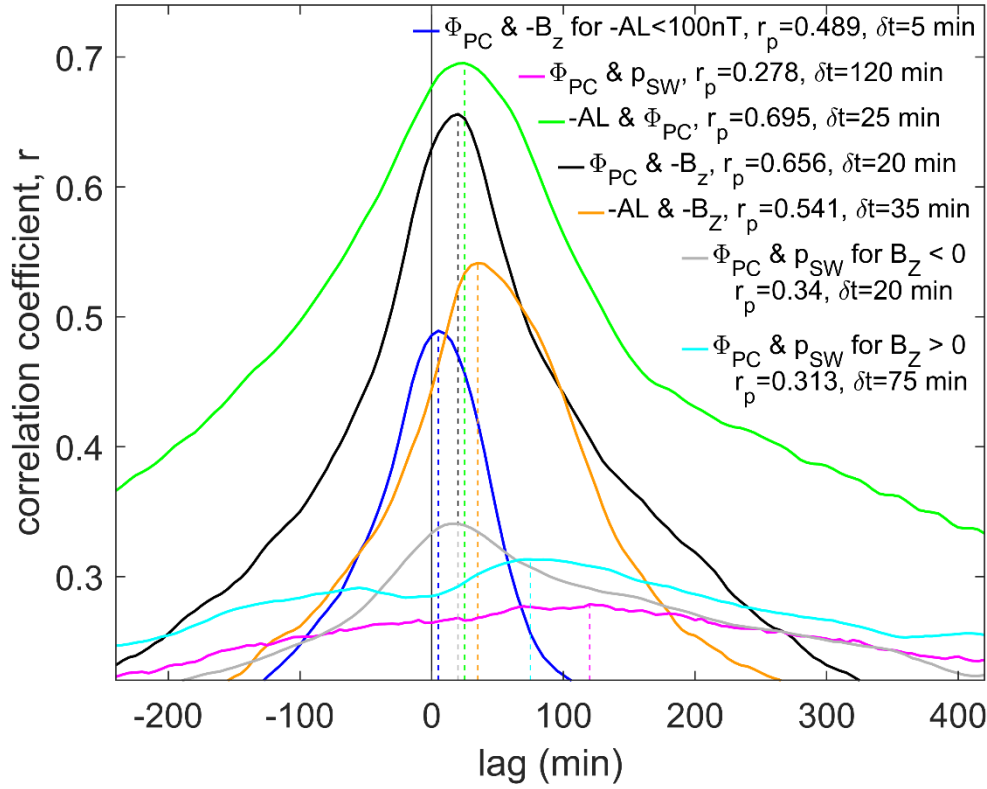
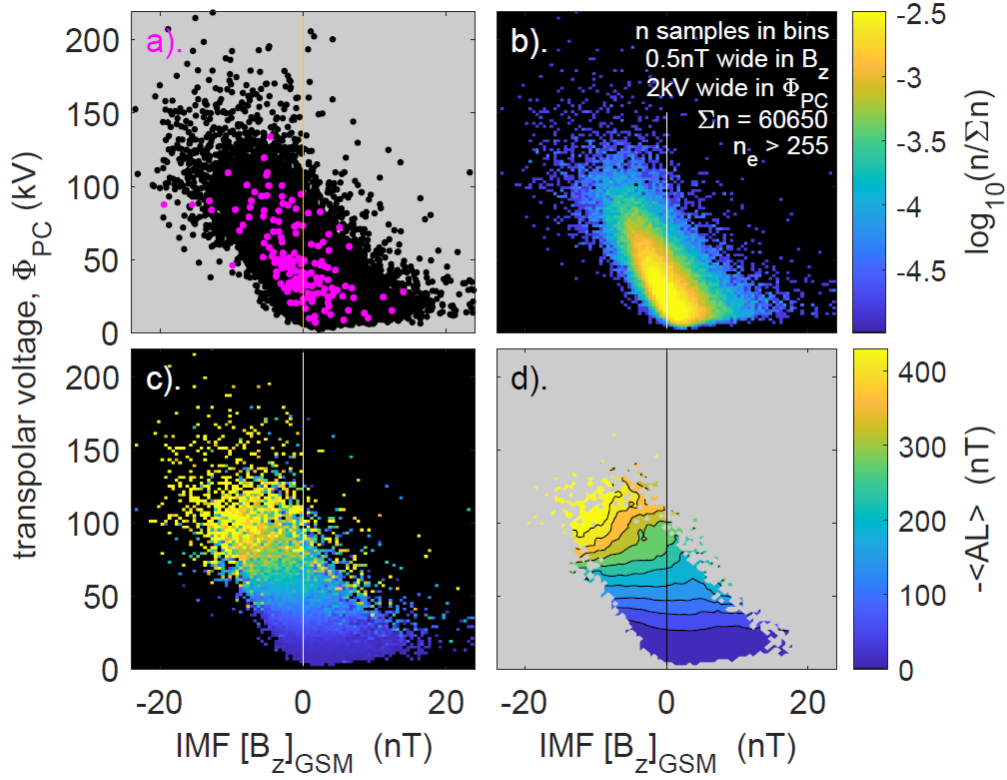


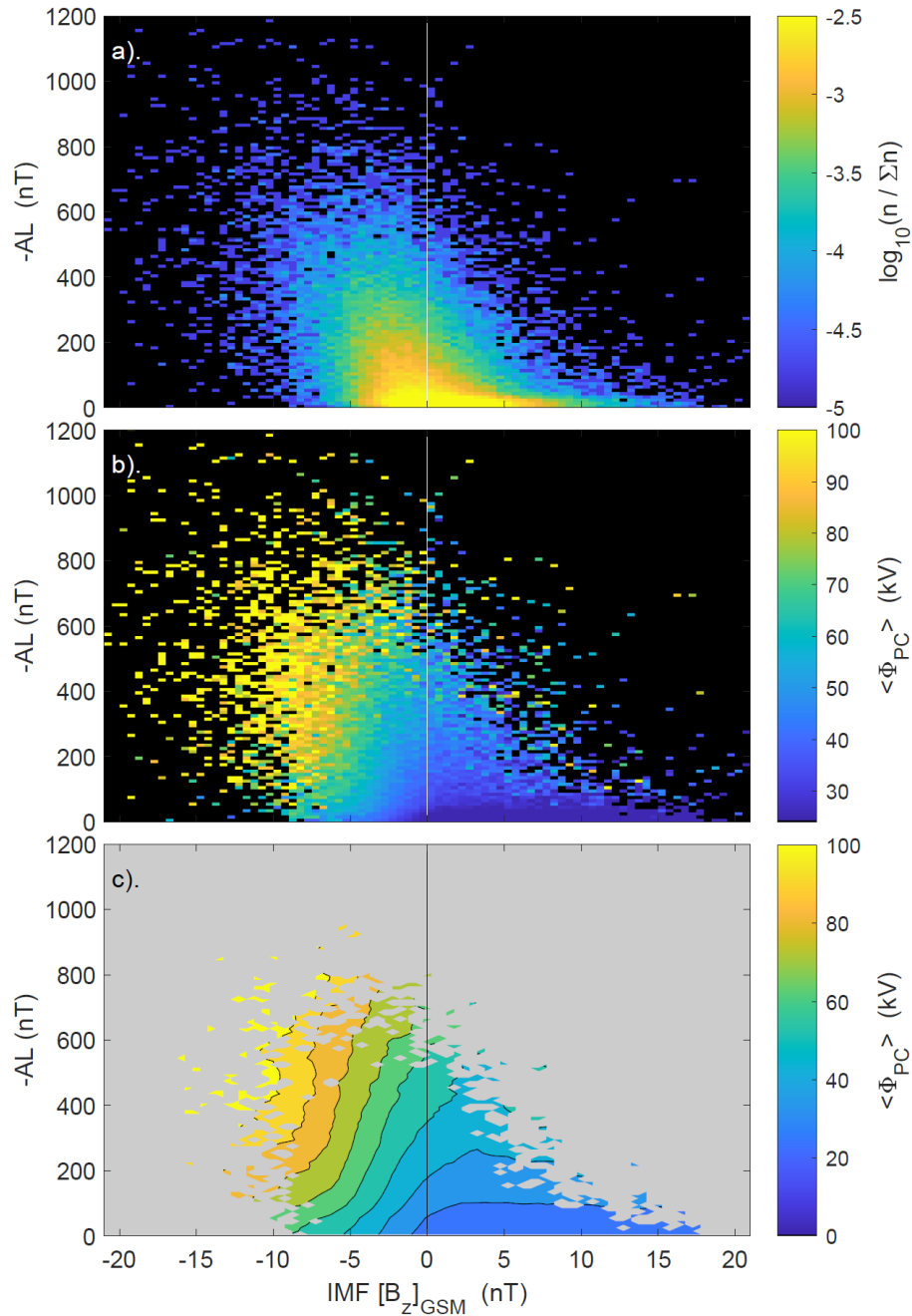
**Figure 6.** Lag correlograms used to determine the optimum lags  $\delta t$ : (black) for  $\Phi_{PC}$  and IMF  $-B_Z$  (in the GSM frame); (blue) for  $\Phi_{PC}$  and IMF  $-B_Z$  (in the GSM frame) for the subset with  $-AL < 100nT$ ; (orange) for the  $-AL$  index and IMF  $-B_Z$ ; (green) the  $-AL$  index and  $\Phi_{PC}$ . The mauve, grey and cyan lines are for  $\Phi_{PC}$  and the solar wind dynamic pressure  $p_{SW}$ : mauve is for all data, grey for southward IMF ( $B_Z < 0$ ) and cyan for northward IMF ( $B_Z > 0$ ). In each case, the first parameter of the pair has been lagged with respect to the second by the lag given by the x-axis. The vertical dashed lines are at the lag  $\delta t$  yielding maximum  $r$ ,  $r_p$ , and the values for  $\delta t$  and  $r_p$  are given for each case in the legend. All data are selected by the  $\Phi_{PC}$  dataset for  $n_e > n_{lim} = 255$  radar echoes.





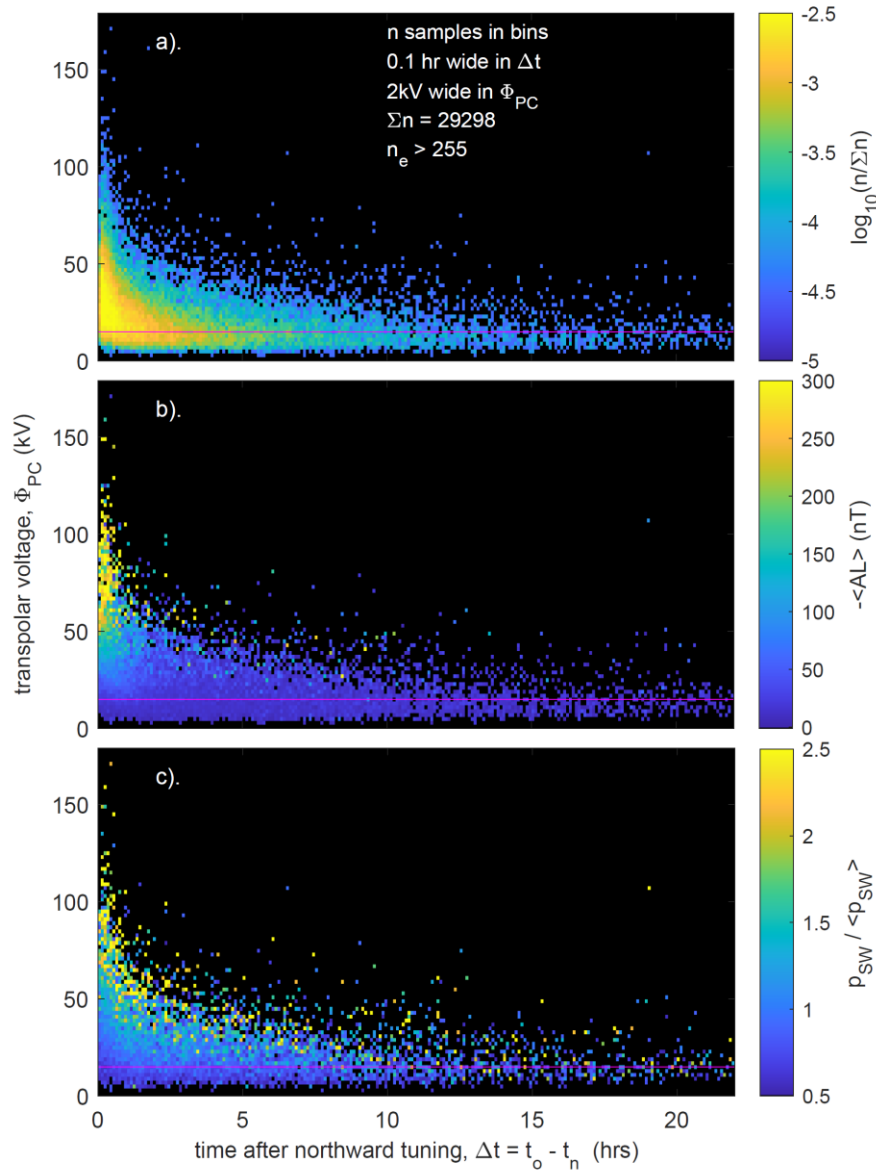
1355

1356 **Figure 7.** (a) Scatter plots of transpolar voltage estimates  $\Phi_{PC}$  as a function of the IMF  $B_z$   
 1357 component. The black points are for the survey of SuperDARN presented here (for  $n_e >$   
 1358 255) and the mauve points are from the survey of data from various spacecraft by Cowley  
 1359 (1984). (b) The fraction of samples  $n/\Sigma n$  (on a logarithmic scale) in bins that are  $\Delta B_z =$   
 1360  $0.5 \text{ nT}$  wide in IMF  $B_z$  (in the GSM frame of reference) and  $\Delta \Phi_{PC} = 2 \text{ kV}$  wide in the  $\Phi_{PC}$ ,  
 1361 as a function of  $B_z$  and  $\Phi_{PC}$ . The IMF  $B_z$  data are 15-minute boxcar running means of 1-  
 1362 min. observations. (c). The mean negative AL index  $-\langle AL \rangle$  in the same bins as used in  
 1363 part (b). In both panels only  $\Phi_{PC}$  values based on  $n_e > 255$  radar echoes are used and bins  
 1364 with no samples are shaded black. Part (d) shows the same data as part (c), fitted with contour  
 1365 levels. Note in relation to Part (a), Cowley (1984) presented the data in terms of the dawn-to-  
 1366 dusk interplanetary electric field,  $E_Y = V_{SW} B_Z$  whereas we here use an  $x$ -axis of  $B_Z =$   
 1367  $E_Y/V_{SW}$ . Also the satellite  $\Phi_{PC}$  data have been scaled to the radar values using the best-fit  
 1368 linear regression shown in part (c) of Figure A1 in Appendix A.



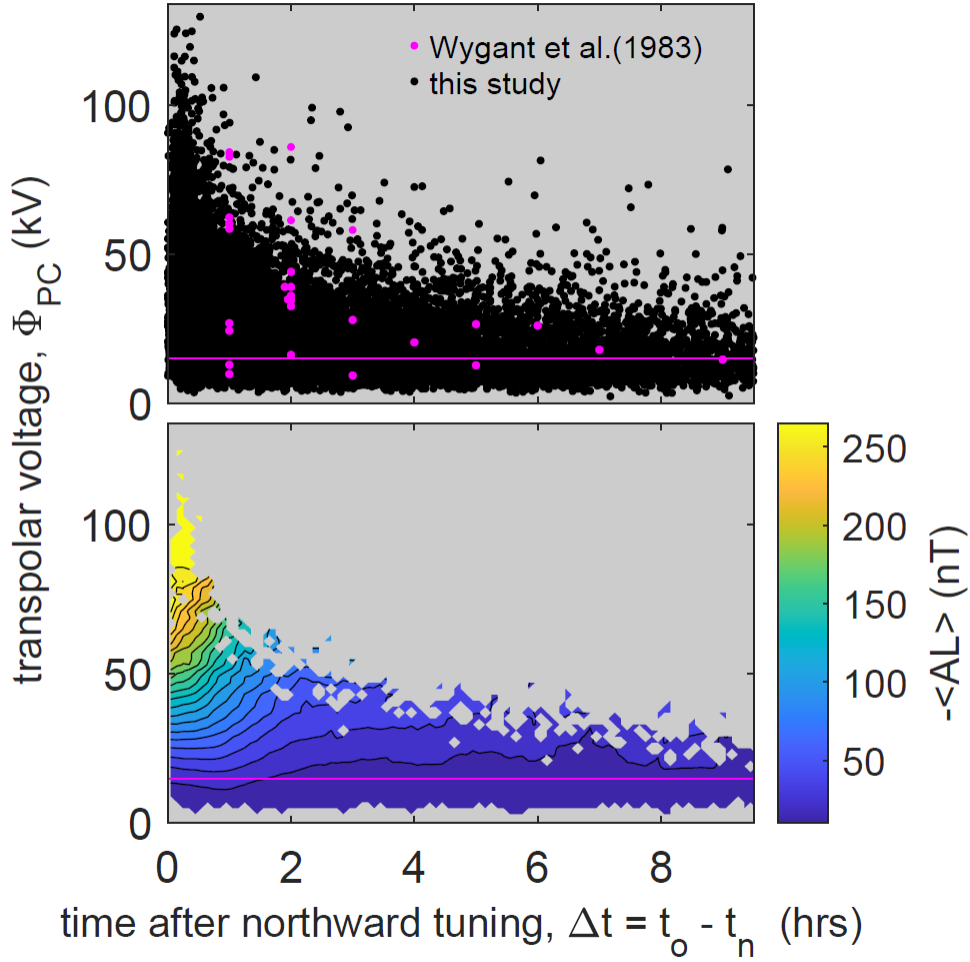
1369

1370 **Figure 8.** Plots on IMF  $B_z$  component and  $AL$  index axes of (a) the fraction of samples  $n/\Sigma n$   
 1371 (on a logarithmic scale) and (b) mean transpolar voltage  $\langle \Phi_{PC} \rangle$  in bins that are  $\Delta B_z =$   
 1372  $0.5 nT$  wide in IMF  $B_z$  (in the GSM frame of reference) and  $\Delta AL = 10 nT$  wide in the  $AL$   
 1373 index, as a function of  $B_z$  and  $-AL$ . Both of  $B_z$  and  $AL$  data are 15-minute boxcar running  
 1374 means of 1- minute observations. Bins with no samples are shaded black. Only  $\Phi_{PC}$  values  
 1375 based on  $n_e > 255$  radar echoes are used. Part (c) shows the same data as Part (b), fitted with  
 1376 contour levels.



1377

1378 **Figure 9.** (a) The fraction of samples  $n/\Sigma n$  (on a logarithmic scale) during continuous  
 1379 northward IMF ( $B_z > 0$  in the GSM frame of reference, using 15-minute boxcar running  
 1380 means of 1-minute IMF data) as a function of  $\Phi_{PC}$  and the time that the IMF has been  
 1381 northward,  $\Delta t = (t_o - t_n)$ , where  $t_o$  is the time of the  $\Phi_{PC}$  observation and  $t_n$  is the time at  
 1382 which the IMF turned northward, in bins that are 0.1 hr wide in  $\Delta t$  and 2 kV wide in  $\Phi_{PC}$ .  
 1383 Bins with no samples are shaded black. (b) The same as (a) for the mean negative AL index  
 1384  $-\langle AL \rangle$ . (c) The same as (a) for the normalised solar wind dynamic pressure,  
 1385  $p_{SW} / \langle p_{SW} \rangle$ . In all there panels only  $\Phi_{PC}$  values based on  $n_e > 255$  radar echoes are used  
 1386 and bins with no samples are shaded black.



1387

1388

1389

1390

1391

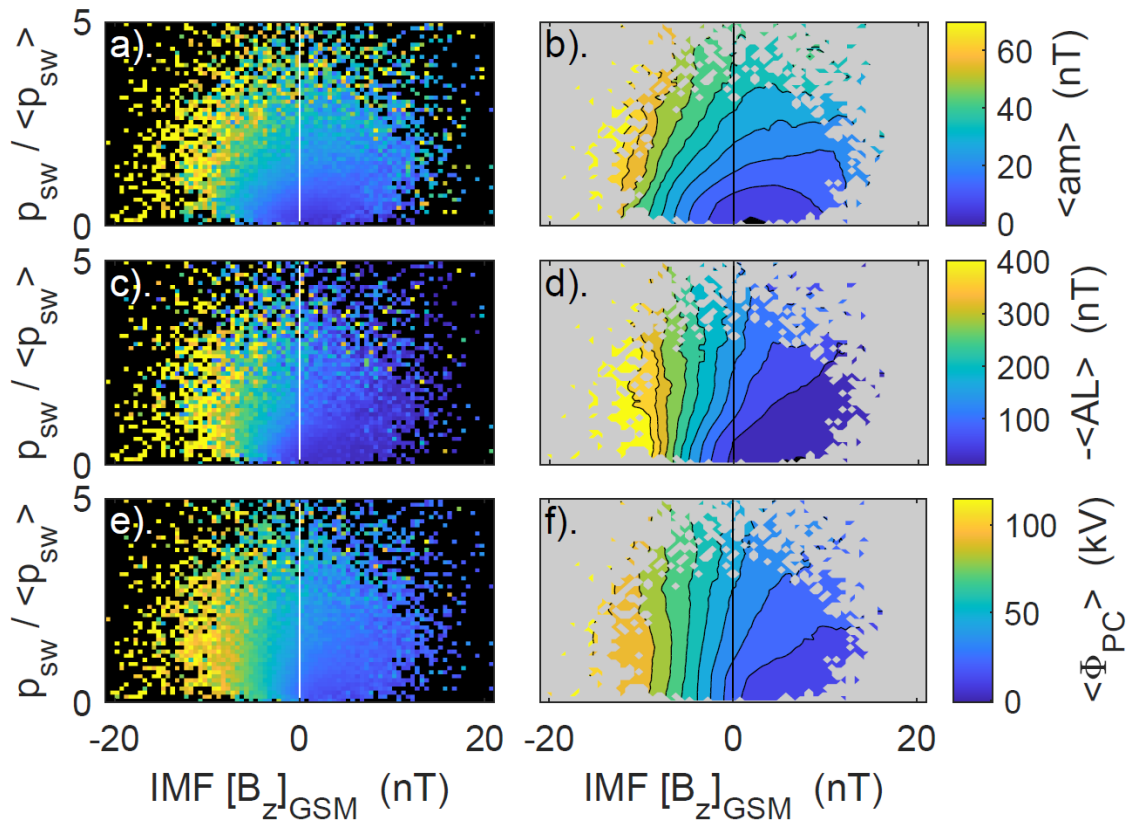
1392

1393

1394

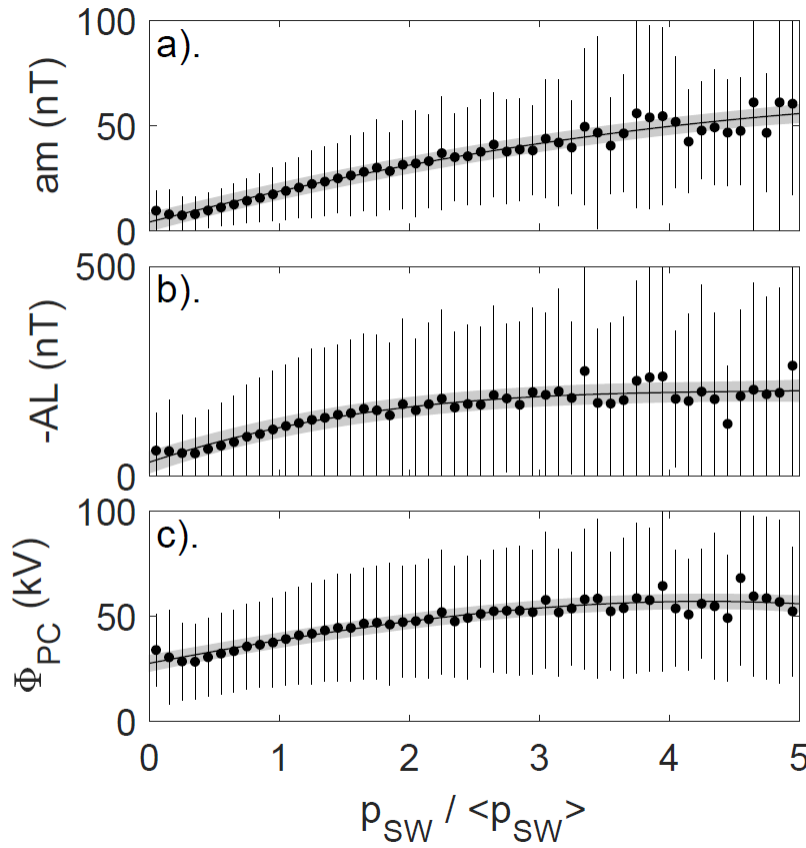
1395

**Figure 10.** Detail of Figure 9 at small times since the IMF turned northward,  $\Delta t = (t_o - t_n)$ , where  $t_o$  is the time of the  $\Phi_{PC}$  observation and  $t_n$  is the time at which the IMF turned northward. The black dots in the top panel form a scatter plot of the  $\Phi_{PC}$  data as a function of  $\Delta t$  from the present survey. The mauve dots are the satellite  $\Phi_{PC}$  data from Wygant *et al.* (1983), which have been scaled to the radar values using the best-fit linear regression shown in part (c) of Figure A1 in Appendix A. The lower panel shows contours of the mean AL index for the data points of the present survey (and so is a contoured version of Figure 9b for small  $\Delta t$ ).



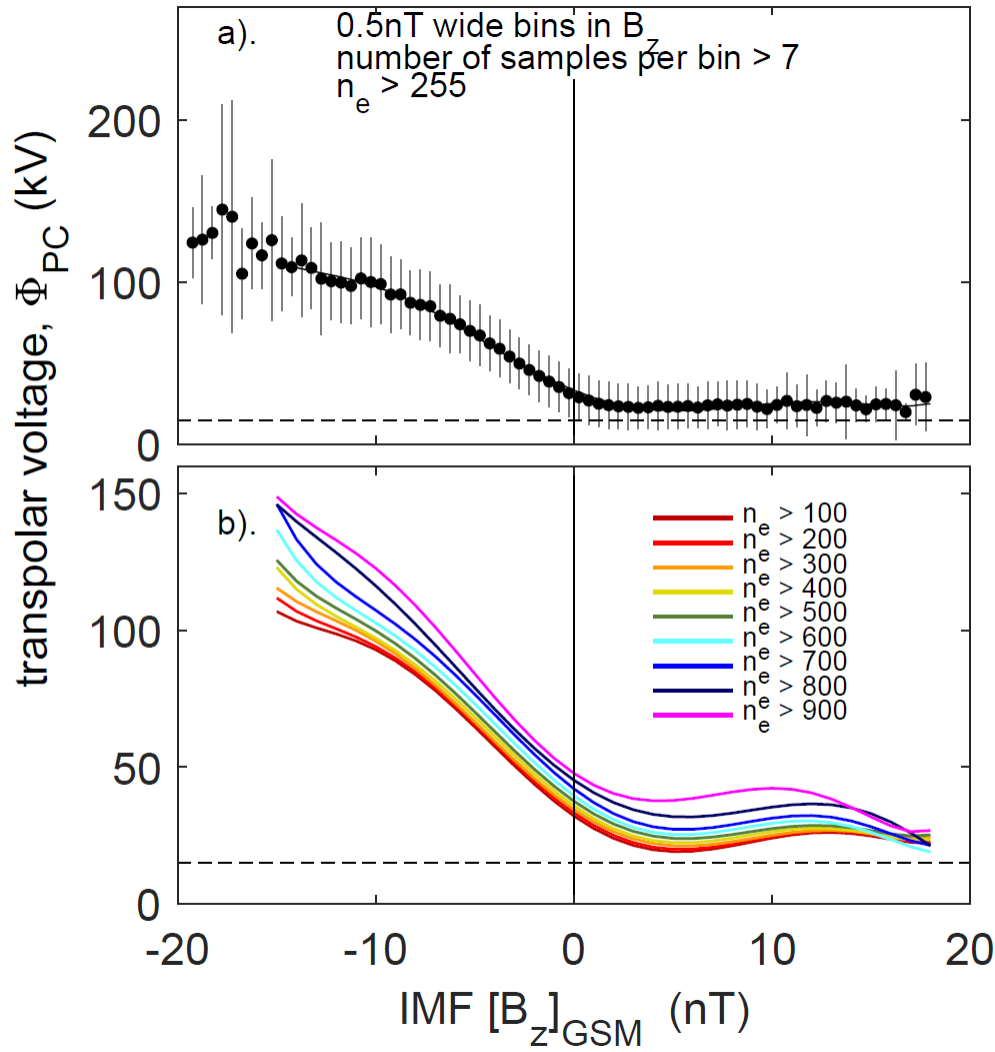
1396

1397 **Figure 11.** The left-hand plots show mean values in bins and the right-hand plots the same  
 1398 data fitted with contours. The top plots (a) and (b) are for the mid-latitude  $am$  geomagnetic  
 1399 range index; the middle plots (c) and (d) are for the mean negative  $AL$  index; and the bottom  
 1400 plots (e) and (f) are for the mean transpolar voltage  $\Phi_{PC}$ . All are as a function of the north-  
 1401 south IMF component ( $B_z$ , defined as positive northward) in the GSM frame of reference and  
 1402 the normalised solar wind dynamic pressure,  $p_{SW}/\langle p_{SW} \rangle$ , where  $p_{SW} = m_{SW}N_{SW}V_{SW}^2$  and  
 1403  $m_{SW}$  is the mean ion mass,  $N_{SW}$  the number density and  $V_{SW}$  the speed of the solar wind and  
 1404 the normalising factor  $\langle p_{SW} \rangle$  is the mean for all data in the 1995-2020 period of this study.  
 1405 The  $AL$ ,  $\Phi_{PC}$ , and  $p_{SW}$  are all 15-minute boxcar running means of 1-minute data whereas the  
 1406  $am$  data are linearly interpolated to the time of the  $\Phi_{PC}$  sample from the raw 3-hourly  $am$   
 1407 data. Bins are  $\Delta B_z = 0.5nT$  wide in IMF  $B_z$  and 0.1 wide in  $p_{SW}/\langle p_{SW} \rangle$ . Bins with no  
 1408 samples are shaded black in the left-hand panels and give areas of grey on the right where the  
 1409 data are too sparse for contours to be fitted. The  $am$ ,  $-AL$ , and  $\Phi_{PC}$  values used were for  
 1410 times of  $\Phi_{PC}$  samples that are based on  $n_e > 255$  radar echoes.



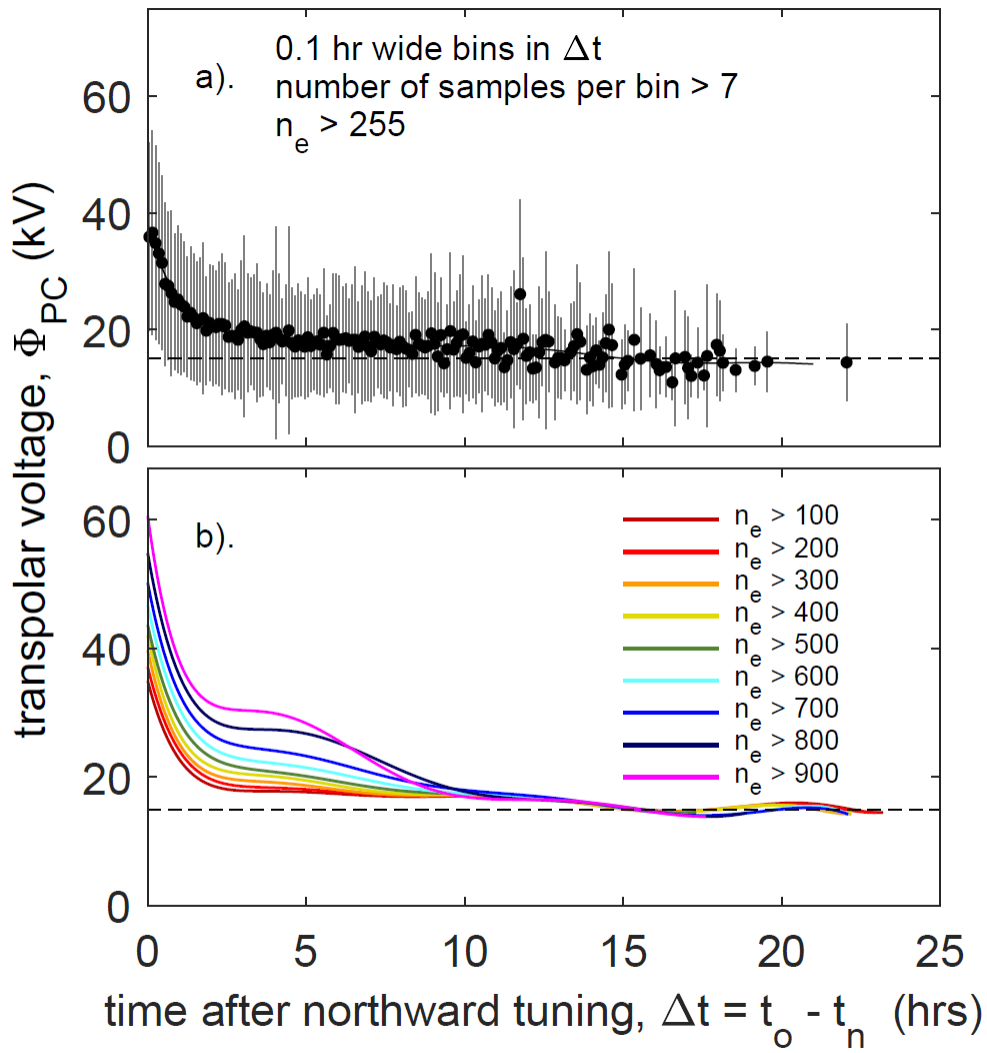
1411

1412 **Figure 12.** Mean values (with uncertainty bars of plus and minus one standard deviation) of  
 1413 (a) the  $am$  geomagnetic range index, (b) the negative  $AL$  index and (c) the transpolar voltage  
 1414  $\Phi_{PC}$  as a function of the normalised solar wind dynamic pressure  $p_{SW}/<p_{SW}>$  in bins that  
 1415 are 0.1 wide in  $p_{SW}/<p_{SW}>$ . The black line is the best 3<sup>rd</sup>-order polynomial fit to the mean  
 1416 values and the grey area around it is bound by plus and minus the 1-sigma error in the fit.  
 1417 The  $am$ ,  $-AL$ , and  $\Phi_{PC}$  values used were for times of  $\Phi_{PC}$  samples that are based on  $n_e >$   
 1418 255 radar echoes.



1419

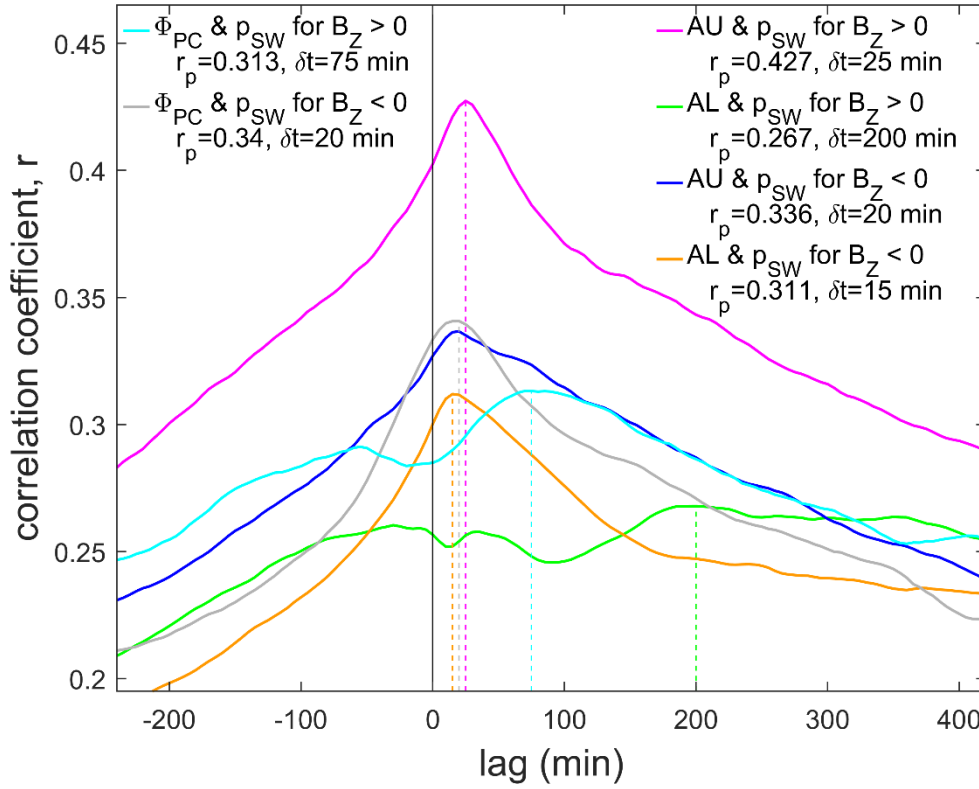
1420 **Figure 13.** (a) Mean values (with uncertainty bars of plus and minus one standard deviation)  
 1421 of the transpolar voltage  $\Phi_{PC}$  as a function of IMF  $B_z$  (in the GSM frame of reference) in bins  
 1422 that are  $\Delta B_z = 0.5\text{nT}$  wide for  $\Phi_{PC}$  samples that are based on  $n_e > 255$  radar echoes. The  
 1423 solid line is a 6<sup>th</sup>-order polynomial fit to the mean values. (b). Analysis of the effect on part  
 1424 (a) of the threshold required for the number of radar echoes,  $n_e$ . The coloured lines are 6<sup>th</sup>-  
 1425 order polynomial fits to the mean values of  $\Phi_{PC}$  for  $n_e$  thresholds of  $n_{lim} = [100:100:900]$   
 1426 that were also used in Figures 4 and 5.



1427

1428 **Figure 14.** (a) Mean values (with uncertainty bars of plus and minus one standard deviation)  
 1429 of the transpolar voltage  $\Phi_{PC}$  during northward IMF as a function of time since the IMF  
 1430 turned northward,  $\Delta t = (t_o - t_n)$  in bins that are 0.1 hr wide:  $t_o$  is the time of the  $\Phi_{PC}$   
 1431 observation and  $t_n$  is the time at which the IMF turned northward.  $\Phi_{PC}$  samples are based on  
 1432  $n_e > 255$  radar echoes. The solid line is a 6<sup>th</sup>-order polynomial fit to the mean values. (b)  
 1433 Analysis of the effect on part (a) of the threshold required for the number of radar echoes,  $n_e$ .  
 1434 The coloured lines are 6<sup>th</sup>-order polynomial fits to the mean values of  $\Phi_{PC}$  for  $n_e$  thresholds  
 1435 of [100:100:900] that were also used in Figures 4, 5 and 13.





1436

1437 **Figure 15.** Lag correlograms for auroral electrojet indices with solar wind dynamic pressure:  
 1438 (mauve) for  $AU$  and  $p_{SW}$  for IMF  $B_Z > 0$  (in the GSM frame); (green) for  $AL$  and  $p_{SW}$  for  
 1439 IMF  $B_Z > 0$ ; (blue) for  $AU$  and  $p_{SW}$  for IMF  $B_Z < 0$ ; and (orange) for  $AL$  and  $p_{SW}$  for IMF  
 1440  $B_Z < 0$ . In each case, the first parameter of the pair has been lagged with respect to the  
 1441 second by the lag given by the x-axis. The vertical dashed lines are at the lag  $\delta t$  yielding  
 1442 maximum  $r$ ,  $r_p$ , and the values for  $\delta t$  and  $r_p$  are given for each case. The cyan and grey lines  
 1443 are the corresponding lag correlograms for the transpolar voltage  $\Phi_{PC}$  and  $p_{SW}$  for IMF  
 1444  $B_Z > 0$  and IMF  $B_Z < 0$ , respectively.

## Appendix A.

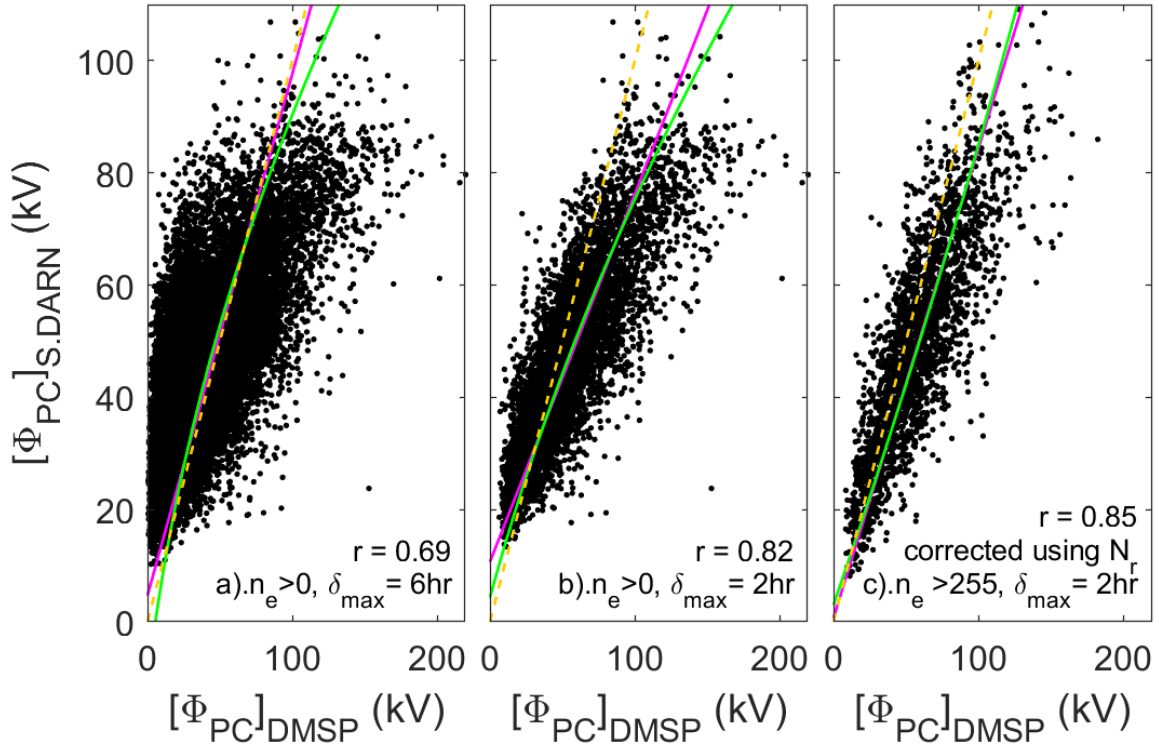
The SuperDARN data used here were processed at the Institute of Space and Atmospheric Studies, University of Saskatchewan, using the SuperDARN Radar Software Toolkit (RST) 4.3 (2019) developed and maintained by the SuperDARN Data Analysis Working Group and available from the Github URL <https://zenodo.org/record/3401622#.YNuIbUwo-1k>

SuperDARN Data Analysis Working Group. Participating members; Thomas, E. G.; Sterne, K. T.; Shepherd, S. G.; Kotyk, K.; Schmidt, M. T.; Ponomarenko, P. V.; Bland, E. C.; Walach, M.-T.; Reimer, A. S.; Burrell, A. G.; Billett, D. D. (2019) SuperDARN Radar Software Toolkit (RST) 4.3, doi: 10.5281/zenodo.3401622

To allow reproduction of the dataset, note that all the RST (version 4.3) defaults were used to create the potential maps, except the following:

- (i) fitacf-version 3.0 was used instead of fitacf-version 2.5
- (ii) -tl 60 (scan time 60 seconds)
- (iii) -c (concatenate grid files)
- (iv) -minrng 10 (include data from minimum range gate 10)
- (v) use -cn a, b, c, d for channel fitacf files (a, b, c, d in the filename), or -cn\_fic A, b for fitacfs with twofsound for channel 0 and 1 for A and channel 2 for B
- (vi) -xtd for extra variable spectral width and SNR
- (vii) -stime 00:00 to give start time at 00:00
- (viii) -vemax 10000 to exclude any data above velocity value of 10,000 ms<sup>-1</sup>
- (ix) -l 50 to set map minimum latitude to 50 degrees
- (x) -if OMNI.txt to use OMNI dataset to drive re-analysis model
- (xi) -d 00:10 for 10 minute delay on the input OMNI data. Note that the results were not sensitive to this value and Figure 6 of the main paper shows that the observed lag between  $\Phi_{PC}$  and IMF  $B_z$  is 20 min and set by the observed radar Doppler shifts and not the model.
- (xii) -o 8 for harmonic order 8
- (xiii) -d l for low doping level. The doping level sets the relative weight given to the model compared to the data and can be set to light, medium and heavy. As we wish the maps to be strongly data-driven, we have set the model doping to light.

1474 We here present an overview plot of the comparisons between SuperDARN and DMSP  
1475 transpolar voltages (respectively  $[\Phi_{PC}]_{\text{S.DARN}}$  and  $[\Phi_{PC}]_{\text{DMSP}}$ ) referred to in the text. (The full  
1476 analysis will appear in the paper Lockwood, M., K.A. McWilliams, and M.R. Hairston,  
1477 Semiannual and Universal Time variations in magnetospheric convection: 1. Transpolar  
1478 Voltage Data, to be submitted to J. Geophys. Res.). These comparisons are for data from  
1479 2001 and 2002 and are for dawn-to-dusk DMSP passes only and consider the effects of both  
1480 the proximity of the satellite path the diameter of the polar cap giving the transpolar voltage in  
1481 the SuperDARN data (quantified by the parameter  $\delta_{max}$ ) and the number of echoes,  $n_e$   
1482 involved in computing  $[\Phi_{PC}]_{\text{S.DARN}}$ .



1484

**Figure A1.** Comparisons of simultaneous (with 30 minutes) transpolar voltage measurements by the SuperDARN radars,  $[\Phi_{PC}]_{S.DARN}$ , and from DMSP satellite passes,  $[\Phi_{PC}]_{DMSP}$ . The scatter plot in (a) is for all data, irrespective of how many radar Doppler shift measurements contributed to the SuperDARN values and the Magnetic Local Times ( $\delta$  values) of the DMSP intersections of the convection reversal boundary (CRB). In (b) the derived stringent criterion for the MLT of the DMSP intersections of the CRB ( $\delta \leq \delta_{max} = 2hrs$ ) has been applied. In (c) The same restriction is applied to the DMSP passes and the number of radar data points,  $n_e$  must exceed 255. On all three plots, the mauve line is the best linear regression, the green line the 2<sup>nd</sup>-order polynomial fit, and the orange dashed line the ideal agreement ( $[\Phi_{PC}]_{S.DARN} = [\Phi_{PC}]_{DMSP}$ ). The correlation coefficient,  $r$ , and the r.m.s. deviation of the two data sets,  $\Delta$ , is given in each case. The number of data points in (a), (b) and (c) are 16714, 6023 and 2468, respectively.